Revision_1

High pressure behavior and structural transition of beryl-type johnkoivulaite, $Cs(Be_2B)Mg_2Si_6O_{18}$

G. Diego Gatta, Martin Ende, Sofija Miloš, Nicola Rotiroti,
Aaron C. Palke, Ronald Miletich

Corresponding author:
G. Diego GATTA
Università degli Studi di Milano, Dipartimento di Scienze della Terra, Via Botticelli 23, I-20133 Milano, Italy – E-Mail: diego.gatta@unimi.it

Manuscript submitted to: The American Mineralogist

High pressure behavior and structural transition of beryl-type johnkoivulaite, $Cs(Be_2B)Mg_2Si_6O_{18}$

G. Diego Gatta[1]*, Martin Ende[2], Sofija Miloš[2], Nicola Rotiroti[1], Aaron C. Palke[3], Ronald Miletich[2]

[1] Università degli Studi di Milano, Dipartimento di Scienze della Terra, Via Botticelli 23, I-20133 Milano, Italy
[2] University of Vienna, Department of Mineralogy and Crystallography, A-1090 Wien, Austria
[3] Gemological Institute of America, Carlsbad, CA 92008, USA

Abstract

The beryl-group mineral johnkoivulaite, $Cs(Be_2B)Mg_2Si_6O_{18}$, was compressed hydrostatically in a diamond-anvil cell up to 10.2 GPa. *In-situ* Raman spectroscopy and X-ray crystallography revealed a *P*6/*mcc*-to-$P\bar{3}c1$ (second-order) phase transition on isothermal compression at the critical transition pressure $P_c = 4.13 \pm 0.07$ GPa. The elastic parameters determined for the volume elasticity of the two polymorphs correspond to a Birch-Murnaghan equation of state with $K_0 = 148 \pm 2$ GPa and $K' = 0$ for $P < P_c$ and $K_0 = 75.5 \pm 0.9$ GPa with $K' = 4$ for $P > P_c$. The low-*P* polymorph shows anomalously linear compression behavior, as reported for several other beryl-derived framework structures. The high-*P* polymorph, which was found to follow a $a' = a \cdot \sqrt{3}$, $c' = c$ superstructure according to $P\bar{3}c1$, is almost twice as compressible as its low-*P* form. This is unique for any beryl-derived structure and can be attributed to the high degree of freedom for atomic displacements in the superstructure. The reduced symmetry can also be understood as the effect of the driving mechanism of the transformation. The extra-framework Cs channel components counteract any lateral deformation of the channels parallel to [0001] within the microporous framework and, similar to pezzottaite, are responsible for maintaining the trigonal/hexagonal lattice metrics.

Keywords: beryl-type structure, johnkoivulaite, high pressure, structural transition, second-order phase transition, superstructure

Introduction

The beryl-type structure is an outstanding structure representing a non-holotetrahedral framework, with a pronounced one-dimensional porosity in the form of channels running along [0001]. It is represented in nature by several beryllium silicate minerals, such as beryl $Be_3Al_2(Si_6O_{18})$, stoppaniite $Be_3Fe_2(Si_6O_{18})$, and bazzite, $Be_3Sc_2(Si_6O_{18})$, whose crystal structures consist of the symmetry-determining $[Si_6O_{18}]^{6-}$ silicate ring units that predetermine the hexagonal archetype microporous framework (*e.g.*, Bragg and West 1926; Gibbs et al. 1968; Artioli et al. 1993; Armbruster et al. 1995; Ferraris et al. 1998; Della Ventura et al. 2000). Any deviation from the beryl-aristotype *P*6/*mcc* symmetry originates from stoichiometric substitution, such as in cordierite $Al_3Mg_2(AlSi_5O_{18})$ and sekaninaite $Al_3Fe_2(AlSi_5O_{18})$, where the substitution of 1/3 of the silicon atoms on the *T*2 site within the ring units, and the simultaneous occupation of Si on the *T*1 site, leads to symmetry-breaking orthorhombic *Cmcm* cation distribution (Armbruster 1985; Redfern et al. 1989; Daniels et al. 1994; Malcherek et al. 2001). While the cation redistribution on the tetrahedral *T*1, *T*2 and the octahedral *M* sites does not affect the total charge balance of the framework, both in pezzottaite, $Cs(Be_2Li)Al_2Si_6O_{18}$, and johnkoivulaite, $Cs(Be_2B)Mg_2Si_6O_{18}$, the stoichiometric substitution of one third of the Be by either lithium or boron at the *T*1 position leads to a formal charge deficiency within the framework (Yakubovich et al. 2009; Gatta et al. 2012; Lambruschi et al. 2014; Palke et al. 2021). This, in turn, requires charge balance through additional extra-framework cations located within the one-dimensionally infinite channel mentioned above. The structures of pezzottaite and johnkoivulaite are characterized by the intercalation of a significant fraction of alkali cations, preferably high Cs contents, within the cavities of the existing one-dimensional channels. At least for pezzottaite, a resultant lower symmetry and the formation of a trigonal superstructure, according to the $R\bar{3}c$ space group, could be demonstrated for the existing Li-Be cation ordering.

The ability to incorporate Cs in the microporous framework makes beryl-type compounds of interest in the materials science community. In particular, immobilization of Cs-137 makes the physicochemical properties of this potential host structure important for possible technological applications. Thermodynamic properties and phase stabilities are an important focus of research. The two most prominent representatives of this mineral group, *i.e.*, cordierite and beryl, moreover are characterized by their petrological importance. Cordierite is a stable phase in contact metamorphic pelitic rocks or in high-grade regionally metamorphosed schists, gneisses, and granulites. Beryl is a host of Be, a rare lithophile element, in highly evolved S-type granites, granitic pegmatites, hydrothermal deposits related to granite (*e.g.*, greisen), volcanogenic hosted beryllium deposits, or metamorphic rocks (*i.e.*, emerald-bearing schists) (Hess 1969; Deer et al. 1992; Spear 1993; Barton and Young 2002; García-Moreno et al. 2007; Klein and Philpotts 2012). Potential phase

transformations, their mechanisms and the knowledge of the factors stabilizing or destabilizing the structure are the subject of numerous investigations under variable pressure and temperature conditions. Among others, the isothermal equations of state as well as thermal expansion coefficients for beryl, cordierite and also pezzottaite have been investigated in the past. In addition to the long-known order-disorder transformations, such as that of cordierite-iolite, transitions under pressure into new, denser polymorphic forms have been reported, including transformation into the heavily twinned triclinic form of cordierite (Miletich et al. 2014a; Finkelstein et al. 2015), the likely formation of modulated beryll-II at pressures beyond 12 GPa (O'Bannon and Williams 2016), or the second-order transition of pezzottaite at 4 GPa from $R\bar{3}c$ to $R3c$ (Ende et al. 2021). A remarkable common feature of all high-pressure investigations is the extraordinary compression behavior with respect to the pressure dependency of the bulk modulus, regardless of whether a transformation was observed or not. In all cases, values for $\partial K/\partial P$ have been determined to be close to zero or even negative, and thus suggest an anomalous elastic behavior for members of this structural family.

The most recently described new mineral species johnkoivulaite is, after pezzottaite, the second and only other representative of the beryl-group with Cs-stuffed host-guest structure required for the stoichiometric charge compensation of the framework. Incorporation of extra-framework components, *e.g.* H_2O, CO_2, Ar or even small fractions of alkali cations, has been reported for some of the mineral phases structurally related to beryl (*e.g.*, Armbruster 1985b,1986; Charoy et al. 1996; Kolesov and Geiger 2000; Mashkovtsev and Thomas 2005). Investigations of static compression, and its dependence on the type and concentration of molecules embedded within channels, also showed a demonstrable influence on the lattice elastic properties (*e.g.*, Miletich et al. 2014a,b; Scheidl et al. 2014). Nevertheless, pezzottaite was investigated as the very first phase with considerable contents of stoichiometrically required extra-framework alkali cations. Despite the analogy regarding the stoichiometric formula, the different symmetry alone is striking, so that high-pressure studies on this new mineral appeared necessary in the context of understanding the extraordinary behavior of this structure type. In order to evaluate the lattice properties and structural changes, *in-situ* high-pressure investigations were carried out on a single-crystal sample from the only so far known johnkoivulaite specimen, as compressed hydrostatically by using diamond-anvil cell techniques.

Materials and methods

Sample material and high-pressure sample environment

All investigations in this study were performed on a small fragment extracted from the original type material from Mogok, Myanmar (type specimen deposited under no. 41653, in the collection of the Gemological Institute of America Museum) as described in Palke et al. (2021). The chemical composition can be assumed to correspond to the formula $(Cs_{0.85}K_{0.10})(Be_{1.88}B_{1.12})(Mg_{1.66}Fe_{0.27}Al_{0.05})Si_{5.98}O_{18}$, as determined earlier by means of electron microprobe analyses, laser ablation ICP-MS analyses and infrared spectroscopy. The investigations were carried out on crystal fragments from a double-sided polished crystal plate (measuring 40 ± 2 µm in thickness), which was fabricated in arbitrary orientation from an unoriented crystal grain. High-pressure sample environment was provided by using an ETH-type diamond anvil cell (Miletich et al. 2000), using anvils with 0.6 mm culets and compressing in either cryogenically loaded argon or a conventional ethanol-methanol mixture as the hydrostatic pressure-transmitting medium. Details on the individual loadings, sample dimensions, the gasket thicknesses and borehole diameters are provided in Table S1 in the supplementary material. Pressures on isothermal compression were calibrated using the established quartz and ruby pressure gauges (Angel et al. 1997; Jacobsen et al. 2008; Scheidl et al. 2016) to within estimated uncertainties of less than ± 0.01 GPa (for quartz) and ± 0.06 GPa (for ruby). For single-crystal X-ray diffraction experiment at ambient atmospheric pressure, the crystal fragment was mounted on a Mitigen Kapton loop.

Raman spectroscopy

High-pressure Raman spectroscopic investigations were carried on crystals compressed in argon up to 10.19 GPa by means of a confocal *Horiba Jobin Yvon LabRAM-HR 800* spectrometer using a Nd:YAG laser source, with a wavelength of 532.05 nm. The spectrometer was equipped with an *Olympus BX41* microscope, and its *Olympus LMPIanFL* N 50× objective with a long working distance of 10.6 mm was used for all measurements with the ETH-type DAC. A total of 64 high-pressure spectra were recorded (a series of 19 spectra on compression and a subsequent series of 45 on decompression), covering a spectral range from 50 to 1250 cm^{-1} Raman shift, at 3 × 60 seconds exposure time per step. For all measurements, a diffraction grating with 600 lines per mm was used. Spectra were acquired using the *LabSpec 6* software (*HORIBA Scientific*) and *Peakfit v.4* (*Systat Software Inc.*) software was used for background subtraction as well as for the determination of the band position. All Raman spectra were fitted with the Gauss-Lorentz-area method.

Single-crystal X-ray diffraction

The unit-cell parameters were determined from measurements on a Stoe AED II diffractometer (Eulerian cradle, graphite-monochromatized Mo-radiation from 50 kV / 30 mA sealed-tube source, point detector). Data acquisition and refinement were performed using the SINGLE software (Angel and Finger 2011). In addition to the sample crystal, a quartz single crystal was added inside the pressure chamber and its cell parameters were measured for precise pressure determination. Applying the 8-position centering mode (King and Finger 1979), both unconstrained and symmetry-constrained unit-cell parameters were determined for 16 pressure points in the range between 0.0001 and 8.41 GPa. Equation-of-state (EoS) parameters were fitted to the *P*-*V* data before and after the supposed critical transition pressure, using the software EoSFit7GUI (Gonzalez-Platas et al. 2016).

X-ray intensity data were collected at 0.0001, 1.65 ± 0.05 and 6.50 ± 0.05 GPa, using a Stoe StadiVari diffractometer system equipped with a Dectris Pilatus 300K detector with a 450µm silicon layer and an air-cooled Incoatec IµS molybdenum microfocus tube (operated at 50 kV / 1 mA, beam diameter of ~110 µm FWHM). Details of the instrument settings for the XRD intensity data collections are summarized in Table S2. The diffraction patterns were indexed and intensities integrated using the X-area 1.72 software (Stoe & Cie GmbH). Integrated intensities were corrected for absorption effects, through DAC components and sample, by using the *ABSORB* code (Angel and Gonzales-Platas 2013).

Crystal structures were refined with *JANA2006* suite (Petricek et al. 2014) using neutral atomic scattering factors of Cs, K, Mg, Fe, B, Be, Si, and O according to the International Tables for Crystallography (Prince 2006). The structure refinements were performed against ***F*** using the structure model previously reported by Palke et al. (2021). Secondary isotropic extinction effect was corrected according to the formalism of Becker and Coppens (1974), implemented in *JANA2006*. Due to ambiguity in the true symmetry, as discussed by Palke et al. (2021), various approaches for structure refinements were carried out in space groups *P*6/*mcc* (192), $P\bar{3}1c$ (163) and $P\bar{3}c1$ (165). The structure solution of the data at 6.50 GPa was performed using the *SUPERFLIP* computer program (Palatinus and Chapuis 2007), applying the charge-flipping algorithm. Statistical parameters and other details pertaining to the final refinements are given in Table S2, the atomic positions and displacement parameters are listed in Table S3 and other relevant structural parameters in Table S4 (and in the CIF).

Results

High-pressure Raman spectra

The reference spectrum at 0.0001 GPa is practically identical to the original Raman spectrum described by Palke et al. (2021), featuring the same resonance bands at corresponding bands positions (at ~1085 cm^{-1}, ~1040 cm^{-1}, ~692 cm^{-1}, ~624 cm^{-1}, ~505 cm^{-1}, ~430 cm^{-1}, ~405 cm^{-1}, ~260 cm^{-1} and ~225 cm^{-1} at ambient conditions, cf. Figure 1). With reference to the existing spectral analyses on beryl, pezzottaite and related mineral structures, the observed bands can be assigned to vibration modes of the Si_6O_{18} rings with or without involvement of neighboring tetrahedral and octahedral units (Hofmeister et al. 1987; Kim et al. 1995; Moroz et al. 2000; Lambruschi et al. 2014; Ende et al. 2021).

The Raman spectrum at ambient conditions exhibits no characteristic Raman band in the low-frequency regime between the system limit (50 cm^{-1}) and 200 cm^{-1} Raman shift. Such a vibrational band was found for pezzottaite around 111 cm^{-1} and was attributed to Cs-O vibrations (Ende et al. 2021). Nevertheless, it is noticeable that in the range that is typical for the highly coordinated Cs and other large alkali atoms, the spectral background increases significantly towards the lowest frequencies at the system limit, an observation that has not been reported by Palke et al. (2021), since their measurements were made in the 200-2000 cm^{-1} frequency range. However, at non-ambient pressures, the maximum corresponding to an intense band located below the 50 cm^{-1} limit becomes visible due to the pressure-induced blueshift (Figure 1). This supposed maximum becomes recognizable above ~3 GPa, but it should probably also exist at lower pressures and cannot be detected due to the lower spectral limit of the Raman spectrometer. While only one clear band can be seen in all spectra up to about 3.5 GPa, the appearance of two further bands located at ~80 cm^{-1} and ~120 cm^{-1} can be observed in all spectra above ~4 GPa. This indicates changes related to the coordination of the Cs site, involving either point symmetry changes or the occurrence of individual Cs sites. It is remarkable that the transition described for pezzottaite also resulted in significant changes in the low-frequency spectral range near the 111 cm^{-1} band, as new bands assigned to the Cs atoms evolved with the reported transition (Figure 1).

Although the apparent changes described at 4 GPa are the most striking in the entire Raman spectrum, there are further indications of changes in other spectral regions that give a clear indication of the presence of a phase transformation. A slight change in the value of pressure dependence of the band position $\partial\nu/\partial P$ is evident for several bands (*e.g.,* for ν(1040) and ν(1085) in Figure 2). A somewhat clearer indication is the splitting of ν(1084), which is easily recognizable from ~4 GPa with two clearly separable maxima and, assigned as Si-O stretching mode, also indicates changes in point symmetry or symmetry of sites related to the Si atoms. Another clear indication are the changes

in the relative intensities of individual bands, *e.g.* the intensity inversion related to the bands at ~405 cm^{-1} and ~340-360 cm^{-1}. In summary, it can be stated that many individual subtle spectral changes are associated with the critical pressure at around 4 GPa. The spectra at pressure below and above this transition point show an overall degree of similarity, so that one can assume that the structural topology is, overall, preserved, and in this case only changes in the overarching symmetry are likely to occur. It should be added that the same changes can be observed in both compression and decompression, without significant hysteresis concerning the critical transition pressure.

Lattice properties and static elasticity

The unit-cell parameters measured at 16 different pressures up to ~8.4 GPa are summarized in Table S5. The least-squares refinements of base vectors were performed in a first step with symmetry-unconstrained parameters in a triclinic setting, in order to determine possible pseudo-symmetries due to symmetry breaking. The symmetry-unconstrained refinements confirmed the hexagonal setting of base vectors with *a* being equal to *b* within the experimental uncertainties, and the angles α, β, and γ showing values close to 90°, 90° and 120°, respectively.

The *P* dependency of unit-cell parameters (Figure 3) reveals a compressional anisotropy with the structure being ~10 % less compressible along the *c*-axis than along the *a*-axis (Table 1), following a pattern of anisotropy similar to that of pezzottaite but different from that of beryl or cordierite (Miletich et al. 2014a,b; Scheidl et al. 2014; Fan et al. 2015; O'Bannon and Williams 2016; Ende et al. 2021). An obvious change in the compression behavior can be observed from the critical pressure of ~4 GPa, as described in the high-pressure Raman spectroscopic investigations. Above the critical transition pressure, a significantly higher compressibility is noticeable both in the bulk and in the individual crystallographic axis directions without the occurrence of a significant discontinuity, which would be typical for a first-order phase transition. Fitting a Birch-Murnaghan EoS (Birch 1947) to the experimental data (Figure 3), the pressure derivatives of the moduli K_0 (for volume) and M_0 (axial) show negative values for the data $\leq$ 3.55 GPa, *i.e.* $M' = \partial M_0/\partial P \approx -8$ for the *c*-axis, and even negative values for the volume with $K' = \partial K_0/\partial P \approx -2 \pm 3$. The occurrence of axial negative values has been previously reported for irradiated and non-irradiated cordierite (Miletich et al. 2014a,b; Scheidl et al. 2014), and pezzottaite (Ende et al. 2021), while studies on beryl itself did not report any anomalous behavior (Fan et al. 2015). Structural instabilities have been reported for isostructural materials associated with remarkable elastic-softening behavior, which can be interpreted as a precursor effect of an impending transition in beryl-type phases (Miletich et al. 2014a,b; Scheidl et al. 2014; Ende et al. 2021).

Fits according to Birch-Murnaghan EoS with constraints on *K'* reveal bulk moduli of 148 ± 3 GPa (with *K'* set to 0) and 75.5 ± 0.9 GPa (with *K'* set to 4) for the respective low- and high-pressure form (Table 1). The aforementioned fixed values of the pressure derivative (*i.e., K'* set to 0 for the low-*P* form and to 4 for the high-*P* form) provided the best figures of merit of the EoS fits. Referring to the Anderson-Anderson relationship (Anderson and Anderson 1970), the bulk modulus of the low-*P* form is very similar to that reported for pezzottaite (K_0 = 152 GPa at V/Z = 341.3 Å^3 per formula unit Z), and plots between those of beryl [K_0 = 180 GPa, V_0/Z = 337.7 Å^3 p.f.u. (Fan et al. 2015)] and cordierite [K_0 = 131 GPa, V_0/Z = 387.9 Å^3 p.f.u. (Miletich et al. 2014a)]. In contrast, the high-pressure form of johnkoivulaite is significantly softer as expressed by the parameters obtained for the fit to the 2nd order Birch-Murnaghan EoS (K'=4), for which the bulk modulus is only 75.5 ± 0.9 GPa at an extrapolated V_0/Z = 358.5 Å^3 p.f.u. (Table 1). Only by simply comparing the volume-related lattice elasticities can it be determined that the low-*P* form of johnkoivulaite and pezzottaite, despite crystallographic differences in terms of symmetry, are similar and behave analogously to the other beryl structures with respect to their compression properties. From these points of view alone, the high-*P* form of johnkoivulaite is outstanding and so far unique, since it deviates significantly from the trend line corresponding to the Anderson-Anderson relationship.

The determination of the point of intersection from the two parameterized equations of state allows the critical transition pressure to be bracketed with a value of 4.13 ± 0.07 GPa, taking into account the uncertainties determined from the fits.

Re-evaluating the crystal structure at ambient conditions

At ambient conditions, diffraction data were successfully indexed with the hexagonal unit-cell as reported by Palke et al. (2021) (*i.e.*, a ~ 9.47 and c ~ 9.05 Å), with reflection conditions consistent with the space group *P*6/*mcc* (192). Cs *vs.* K fraction at the *Cs* site, Mg *vs.* Fe fraction at the *Mg* site, and B *vs.* Be fraction at the *Be* site were refined, providing values in good agreement with those previously reported by Palke et al. (2021). Convergence was rapidly archived after a few cycles of refinement, without any significant correlation among the refined variables or anomalous residuals in the difference-Fourier function of the electron density. Any of the conventional parameters validating the structure refinement in *P*6/*mcc* (*i.e.*, *R(F)* and *wR*(*F*) for $I_o > 3\sigma(I_o)$ are, respectively, 1.36% and 2.09%, Table S2 and CIF) leaves no doubt about the correctness of the structure determination and the previous choice of the space group (Palke et al. 2021). In addition, all anisotropic displacement ellipsoids were positive definite. The most anisotropic ones are those of the *O1* and *O2* sites, as already reported by Palke et al. (2021), which appears to be a common feature of

the bridging oxygen atoms in cyclosilicates with corner-sharing polyhedra that confine a channel [*e.g.*, beryl (Gatta et al. 2006); cordierite (Cohen et al. 1977); pezzottaite (Gatta et al. 2012)].

Nevertheless, an ordering of the Be and B cations, which lie at the 6*f* site in *P*6/*mcc*, is to be expected, theoretically in tandem with a lowering of symmetry, corresponding to a subgroup symmetry of the parental *P*6/*mcc*. On the other hand, the real differences between the two X-ray scattering curves of Be and B are so marginal that, regardless of their ordering state, the relevant structure factors have values that are insignificantly different and, therefore, possible differences simply cannot be detected. An apparent analogy to pezzottaite regarding the cation order on the respective *T* site [*i.e.*, ~2/3 Be and ~1/3 Li, as shown by Yakubovich et al. (2009), Gatta et al. (2012), and Ende et al. (2021)] suggests the existence of a comparable *R*-centered superstructure (*i.e.*, $R\bar{3}c$ (167), a = ~15.9 and c = ~27.8 Å, corresponding to $a_{\text{pezzottaite}} = a_{\text{beryl}}\cdot\sqrt{3}$, $c_{\text{pezzottaite}} = 3\cdot c_{\text{beryl}}$). Careful inspection on the reciprocal space, as reconstructed from the recorded frames, did not provide any evidence for the existence of comparable superstructure reflections, either in terms of triplication of the *c*-axis or in terms of significant intensities at the reciprocal lattice points located on (3*n*+1)/3 or (3*n*+2)/3 relative to the base vectors of the beryl-type subcell.

Careful inspection on the reflection statistics shows, for the measurement at 0.0001 GPa, three forbidden reflections with $I_o > 3\sigma(I_o)$ for the reflection class *h0l*, hinting at the existence of a *c*-glide plane parallel to (*h0l*). Any violation of the zonal extinctions in the reflection classes *h0l* and *hhl*, attributed to the existence of the two *c*-glide mirror planes, cannot be confirmed without doubt due to the low number of violating reflections and low values for the observed intensities as expressed by the $I/\sigma(I)$ values. Due to the excellent crystal quality with only minor lattice mosaicity, there is a certain possibility that multiple diffraction (in the sense of a Renninger effect) can also be responsible for the subtle violation of the extinction conditions. Based on a possible direct group-subgroup relationship, the trigonal space group $P\bar{3}1c$ (163) or even merohedral twinning following *Cccm* (66) symmetry might be likely. Attempts to refine the data sets collected within this study did not provide any significant evidence for alternative space-group symmetries. Again, the existence of superstructure reflections can be ruled out and, moreover, none of the available measurements could detect any of the diffuse scattering as described for pezzottaite (Ende et al. 2021), which seems plausible due to the higher degree of order inside the channels due to the lower Cs deficiency and the lack of significant Na contents.

Determination of the high-pressure crystal structure

Diffraction data collected at 6.50 ± 0.05 GPa showed that the high-*P* polymorph is metrically trigonal based on a hexagonal setting, but with different base vectors compared to the low-*P* polymorph, corresponding to *a* ~16.13 Å and *c* ~ 8.85 Å. The metrical relationship between the unit-cells of the different polymorphs is shown in Figure 4, and explains the appearance of superstructure reflections in the reciprocal space. In Figure 5, relevant sections of reconstructed reciprocal space allow a direct comparison of the diffraction data obtained at 1.65 and 6.50 GPa. In order to define the real symmetry of the high-*P* polymorph, a series of tests have been performed considering the possible space groups generated by group-subgroup relationships with the parental one *P*6/*mcc*. The best figure of merit was obtained with the point groups $\bar{3}m1$ and $\bar{3}$. The space group $P\bar{3}c1$ (165) was finally selected, with twinning of two individuals metrically related by (0 1 0, -1 -1 0, 0 0 1) and a twin ratio of 0.5:0.5. A lower symmetry, with space group $P\bar{3}$ (147) cannot be ruled out, but a stable structure refinement was not possible due to the high number of variables.

Compared to the low-*P* polymorph, symmetry lowering of the high-*P* one leads to a structural model with two independent (Cs+K) sites (*i.e.*, *Cs1* and *Cs2*), two independent (Mg+Fe) sites (*i.e.*, *Mg1* and *Mg2*), three unique sites fully populated by Si (*i.e.*, *Si1*, *Si2* and *Si3*), nine unique sites occupied by O (*i.e.*, *O1a*-*O1f* and *O2a*-*O2c*) and two (B+Be) sites (*i.e.*, *Be1* and *Be2*) (Table S3 and CIF). The fraction of Cs and K at the *Cs1* and *Cs2*, along with that of Mg and Fe at *Mg1* and *Mg2*, were successfully refined (with an excellent agreement to the refinement at room conditions, Table S3 and CIF); the fraction of B and Be at the *Be1* and *Be2* sites were fixed to 1/3 and 2/3, respectively. While at 0.0001 GPa the structure was modelled with anisotropic displacement parameters for all the atomic sites, at 1.65 GPa only the atomic sites with greater X-ray scattering factors (populated by Cs/K, Si and O) were refined with anisotropic displacement parameters, and at 6.50 GPa only the *Cs1* and *Cs2* sites were modelled anisotropically for the trigonal structure model. Despite the increase of the refined parameters of the high-*P* polymorph, the structure refinement was conducted with a reasonable ratio between the number of observed structure factors versus the number of refined parameters (~9.8) (Table S2 and CIF). At the end of the refinement [with $R(F_{obs})$ = 0.0560, 55 refined parameters and 540 observed reflections], converge was achieved, and the variance-covariance matrix showed no significant correlation between the refined parameters. The highest/lowest residuals in the difference-Fourier synthesis of the electron density (*i.e.*, +/-2.5 e^{-}Å^{-3}) are due to substantial local disorder in the population of the *Cs1* and *Cs2* sites, along [0001].

The resulting interpolyhedral bond distances are presented in Table S4. Comparing the structures in *P*6/*mcc* and $P\bar{3}c1$, it can be seen that neither the bonding topology nor the polyhedra themselves within the framework undergo significant changes. Bond distances show insignificant variations and the *Si*, *Be* (=Be,B), and *Mg* (=Mg,Fe) polyhedra can be considered as more or less rigid units. The same applies to the coordination environment of the Cs atoms, which are hosted on two independent sites, with the 12-fold coordination split into 6+6 or 4x3 Cs-O bonds. The most important aspect of changes relates to the symmetry reduction of the point symmetries of the special sites of all cations and of *O2*. This concerns in particular: *Cs* (Wyckoff site 2*a*, point symmetry 622) transforming into *Cs1* (2*a*, 32.) and *Cs2* (4*d*, 3..); *Si* (12*l*, *m*..) into *Si1* + *Si2* + *Si3* (each 12*g*, 1); *Mg* (4*c*, 3.2) into *Mg1* (6*f*, .2.) + *Mg2* (6*f*, .2.), *Be* (6*f*, 222) into *Be1* (12*g*, 1) + *Be2* (6*f*, .2.), and *O2* (12*l*, *m*..) into *O2a* + *O2b* + *O2c* (each 12*g*, 1). The degrees of freedom associated with these symmetry reductions also allow the structure to relax with atomic shifts that were previously not permitted as due to symmetry constraints. The only recognizable differences relate to displacive deformations of the framework, which are expressed in individual inter-polyhedral bond angles. The most prominent distortion concerns the ring elements, which no longer follow the strict hexagonal symmetry but adopt a (di)trigonal arrangement (Figure 6).

Mechanism of the pressure-induced phase transition

The evolution of the unit-cell volume of johnkoivulaite with *P* (even considering a normalised volume in order to account for the new metrics of the high-*P* polymorph) shows that the *P*-induced transition at ~4 GPa does not imply any remarkable discontinuity. A phase transition without any volume discontinuity can be considered as to be a second-order (or a tricritical) transformation. An isosymmetric phase transition would have been expected to be first-order in character (*e.g.*, Christy 1995). In this light, a change of symmetry is associated with the transition from the low-*P* to the high-*P* polymorph of johnkoivulaite. The symmetry breaking associated with the *P*6/*mcc*-to-$P\bar{3}c1$ transition determines the change of the lattice periodicity within the lattice-plane direction perpendicular to the *c*-axis. The related triplication of the unit-cell volume of the high-*P* polymorph can be easily understood considering the splitting of the parental *Cs* site (at 0,0,1/4) into two independent sites, *i.e.*, *Cs1* (at 0,0,1/4) and *Cs2* (at 2/3,1/3,0.246). This also goes hand in hand with the observed changes in the Raman spectra, where there are corresponding splittings in the range of the low-frequency bands that can be assigned to the Cs polyhedra, which in turn can be attributed to the lowered point symmetry and the distribution of Cs atoms on two independent sites.

The symmetry lowering of the high-*P* polymorph, with a consequent increase of the degrees of freedom of structural deformation, allows a higher distortion of the coordination polyhedra of the

high-*P* polymorph, as can be deduced by the intra-polyhedral bond distances and angles (Table S4 and CIF). However, a clear picture of the distortion is partially hindered by the lower quality of the post-transition intensity data set and, then, of the structure refinement, with a general increase of the estimated standard deviation on lengths and angles. A pronounced distortion is observed only for the *Be1*-tetrahedron, but this can also be the effect of a more difficult detection of low scatterers (*i.e.*, B, Be) from the high-*P* dataset. As johnkoivulaite contains crystallographic sites with a multi-element population (*i.e.*, Cs+K, Mg+Fe, B+Be); it is presumable that a phase transition, aimed to rearrange the structure with an ordered distribution of the elements in distinctive sites, occurs. However, in this case, the high-*P* polymorph appears to preserve the disorder. In fact, a potential Cs *vs.* K ordering into the [0001] channel would lead to a high-*P* polymorph with a drastically longer *c* axis (as Cs/K ~ 4/1), but johnkoivulaite does not show such a behavior. Similar consideration could be extended to octahedral or tetrahedral sites with multi-element populations.

Diffusion-related ordering does not seem to drive the phase transition at high-pressure, which is not plausible from an energetic point of view, considering that changes occur under isothermal conditions. Furthermore, a comparative analysis of the high-*P* behavior of other cyclosilicates [*e.g.*, beryl (Prencipe et al. 2011; O'Bannon and Williams 2016); pezzottaite (Ende et al. 2021); cordierite (Miletich et al. 2014a,b; Scheidl et al. 2014; Finkelstein et al. 2015)] show that all of them experience *P*-induced phase transitions towards lower symmetry. These transitions are driven by displacive deformation within structural building blocks, which exhibit higher degrees of freedom associated with the loss of local symmetry elements. This also applies, in general, to other ring silicates, such as benitoite, $BaTiSi_3O_9$ (Hejny et al. 2012), which undergoes a similar transition pathway in a displacive second-order phase transition, with the high-pressure polymorph being more compressible than the low-pressure form. In a comparable way, a superstructure is also formed with the phase transition.

The noticeable changes for the cations with the highest coordination are, therefore, only a consequence of the fact that these large cations, such as Cs here in the johnkoivulaite, have the greatest flexibility with regard to steric-geometric adaptations of the coordination polyhedron. Even in the high-*P* polymorph of johnkoivulaite, the new sites have a different bonding scheme showing a 6+6 coordination for *Cs1* (6x ~3.43 Å, 6x ~3.35 Å), whereas the *Cs2* site shows a 3+3+3+3 bonding geometry (max: ~3.55 Å, min: ~3.14 Å) (Table S4 and CIF). It compares to a regular 12-fold coordination in the parental configuration of the low-*P* polymorph (12x *Cs-O2*, with bond length of ~3.40 Å at 0.0001 GPa and ~3.39 at 1.65 GPa) (Table S4 and CIF). Ultimately, however, the change in the channels seems to be only a consequence of the optimization of the framework's compression mechanism, which, in turn, drives the change of symmetry.

Discussion and Implications

The high-pressure form of johnkoivulaite is a new phase with respect to its crystallographic structure, unique among all representatives with respect to the space group at the given lattice periodicity ($P\bar{3}c1$, $a = a_{beryl}\cdot\sqrt{3}$, $c = c_{beryl}$). Trigonal superstructures derived from the aristotype beryl subcell occur, so far, only in Cs-stuffed frameworks, which means that they have been exclusively described for pezzottaite and H*P*-johnkoivulaite. Despite the stoichiometric analogies, *i.e.*, the substitution of one third of the Be atoms by Li or B and the associated charge compensation by additional Cs ions within the [0001]-channel, the two structures follow fundamentally different ordering schemes in terms of lattice periodicities and space groups. The compression behavior of the trigonal high-pressure form determined in this study is also unique compared to all other phases whose structure is derived from the beryl aristotype. H*P*-johnkoivulaite shows about twice the compression (K_0 = ~76 GPa) compared to all topologically isostructural polymorphs, while all other structures are significantly stiffer, thus exhibiting compression modules that range from ~131 to ~180 GPa.

Our study shows that the phase transformation observed has all the properties of a second-order transition, which is clearly displacive. While the symmetry of the high-pressure phase can be determined unequivocally, the theoretical group-subgroup relationships raise doubts about the correctness of the *P*6/*mcc* symmetry of the low-*P* polymorph. With respect to group-subgroup relationship, one can notice that $P\bar{3}c1$ with $a'=a\sqrt{3}$ and $c'=c$ is not a maximal subgroup and it would involve an intermediate $P\bar{3}1c$ (with $a'=a$ and $c'=c$) step. The intermediate $P\bar{3}1c$ is a *translationsgleiche* t2 subgroup (index 2) of *P*6/*mcc*, while the $P\bar{3}1c$ to $P\bar{3}c1$ follows a *non-translationsgleiche* isomorphic i3 group-subgroup relation (index 3), with the observed changes in the base-vector setting that involve a triplication of the unit-cell volume. The possible observation of weak-intensity forbidden reflections in the *h0l* and *hhl* reflection classes might be indicative of the supposed non-hexagonal symmetry and that the hexagonal beryl-type structure of the low-*P* phase represents only an average structure. However, we cannot exclude that the *P*-induced *P*6/*mcc*-to-$P\bar{3}c1$ phase transition is actually a weakly first-order transformation, and that the discontinuity in the *P vs*. *V* path is not so pronounced to be detected. Similarly, we cannot exclude the possibility that a transient step occurs between the *P*6/*mcc* and $P\bar{3}c1$ polymorphs, with an additional polymorph with a very narrow stability field in pressure, whose symmetry and metrical relationships can be consistent with the low- and high-polymorphs observed here in terms of group-subgoup relationship.

The findings of our investigations on only the second example of a Cs-stuffed beryl structure suggest an influence of the channel fillings on the stability of the framework under pressure. In contrast to frameworks that are either empty or only partially occupied by intercalated molecules on partially occupied sites, the large alkali atoms seem to play an important role on the stabilization of the framework, as observed in other open-framework materials [i.e., the so-called "pillar effect" (Gatta et al. 2018)]. These relatively large extra framework components prevent a pressure-induced collapse of the channels, as has been described for the structures of beryl and cordierite, where the formation of modulated structures or highly twinned microstructures of low-symmetrical crystal domains with corresponding deformation of the channel geometries takes place. As also seen with pezzottaite, the incorporation of the Cs atoms seems to bring about a stabilization of the channels with regard to their symmetry, to counteract an elliptical deformation, and thus also to be responsible for maintaining a highly symmetrical framework structure. This is an important prerequisite if one actually wants to consider the beryl-type structure as a host phase for radiogenic Cs-137 and also wants to avoid instability under mechanical stress for such a stable host phase. These aspects of structural stability are an important prerequisite for being able to guarantee the immobility of isotopes with regard to possible technological use.

Acknowledgements

We are grateful to Andreas Wagner (IfMK, University of Vienna) for all the effort in the sample preparation. We thank University of Vienna for financial support within the scope of the grants BE532003 and IP532022 and the Italian Ministry of Education (MIUR) through the project ''PRIN2017 - Mineral reactivity, a key to understand large-scale processes" (2017L83S77). G. Bromiley, an anonymous Reviewer and the Structures Editor Team are warmly thanked for the revision of the manuscript.

References

Anderson, D.L., and Anderson, O.L. (1970) Brief report: The bulk modulus-volume relationship for oxides. Jornal of Geophysical Research, 75, 3494–3500.

Angel, R.J., Allan, D.R., Miletich, R., and Finger, L.W. (1997) The Use of Quartz as an Internal Pressure Standard in High-Pressure Crystallography. Journal of Applied Crystallography, 30, 461–466.

Angel, R.J., and Finger, L.W. (2011) SINGLE : a program to control single-crystal diffractometers. Journal of Applied Crystallography, 44, 247–251.

Angel, R., and Gonzalez-Platas, J. (2013) *ABSORB-7* and *ABSORB-GUI* for single-crystal absorption corrections. Journal of Applied Crystallography, 46, 252–254.

Artioli, G., Rinaldi, R., Ståhl, K., and Zanazzi, P.F. (1993) Structure refinement of beryl single-crystal neutron and X-ray diffraction. American Mineralogist, 78, 762-768.

Armbruster, T. (1985a) Crystal structure refinement, Si,Al-ordering, and twinning in "pseudohexagonal" Mg-cordierites. Neues Jahrbuch für Mineralogie Monatshefte, 6, 255-267.

Armbruster, T. (1985b) Ar, N_2, and CO_2 in the structural cavities of cordierite, and optical and X-ray single-crystal study. Physics and Chemistry of Minerals, 12, 233-245.

Armbruster, T. (1986) Role of Na in the structure of low-cordierite: A single-crystal X-ray study. American Mineralogist, 71, 746-757.

Armbruster, T., Libowitzky, E., Auernhammer, M., Bauerhansl, P., Hoffmann, C., Irran, E., Kurka, A., Rosenstingl, H., and Diamond, L. (1995) Crystal chemistry and optics of bazzite from Furka-basistunnel (Switzerland). Mineralogy and Petrology, 52, 113–126.

Barton, M.D., and Young, S. (2002) Non-pegmatitic Deposits of Beryllium: Mineralogy, Geology, Phase Equilibria and Origin. Reviews in Mineralogy and Geochemistry, 50, 591–691.

Birch, F. (1947) Finite elastic strain of cubic crystals. Physical Review, 71, 809–824.

Bragg W.L. & West, J. (1926) The structure of beryl, $Be_3Al_2Si_6O_{18}$. Proceedings of the Royal Society of London - Series A, Mathematical and Physical Sciences, 111, 691–714.

Cohen, J.P., Ross, F.K., and Gibbs, G.V. (1977) An X-ray and neutron diffraction study of hydrous low cordierite. American Mineralogist, 62, 67–78.

Christy, A. (1995) Isosymmetric Structural Phase Transitions: Phenomenology and Examples. Acta Crystallographica, B51, 753-757

Becker, P. J., and Coppens, P. (1974) Extinction within the limit of validity of the Darwin transfer equations. I. General formalism for primary and secondary extinction and their applications to spherical crystals. Acta Crystallographica, A30, 129-147.

Charoy, B., De Donato, P., Barres, O., and Pinto-Coelho, C. (1996) Channel occupancy in an alkali-poor beryl from Serra Branca (Goias, Brazil): Spectroscopic characterization. American Mineralogist, 81, 395–403.

518 Daniels, P., Wunder, B., Sahl, K., and Schreyer, W. (1994) Changing lattice metrics of synthetic
519 cordierites: the metastable hexagonal to orthorhombic transformation sequence during isothermal
520 annealing. European Journal of Mineralogy, 6, 323-335.

521 Deer, W.A., Howie, R.A., and Zussman, J. (1992) An introduction to the rock-forming minerals. 2nd
522 edition, Longman Scientific & Technical, London, UK, 696 p.

523 Della Ventura, G., Rossi, P., Parodi, G.C., Mottana, A., Raudsepp, M., and Prencipe, M. (2000)
524 Stoppaniite, $(Fe,Al,Mg)_4(Be_6Si_{12}O_{36})\cdot(H_2O)_2(Na,\square)$ a new mineral of the beryl group from Latium
525 (Italy). European Journal of Mineralogy, 12, 121–127.

526 Ende, M., Gatta, G.D., Lotti, P., Grandtner, A., and Miletich, R. (2021) $Cs(Be_2Li)Al_2Si_6O_{18}$, a
527 cesium-stuffed host-guest structure, and its structure-property variations with temperature and
528 pressure. Journal of Solid State Chemistry, 293, 121841.

529 Fan, D., Xu, J., Kuang, Y., Li, X., Li, Y., and Xie, H. (2015) Compressibility and equation of state of
530 beryl ($Be_3Al_2Si_6O_{18}$) by using a diamond anvil cell and in situ synchrotron X-ray diffraction.
531 Physics and Chemistry of Mineals, 42, 529–539.

532 Ferraris, G., Prencipe, M., and Rossi, P. (1998) Stoppaniite, a new member of the beryl group: crystal
533 structure and crystal-chemical implications. European Journal of Mineralogy, 10, 491-496.

534 Finkelstein, G., Dera, P., and Duffy, T. (2015) High-pressure phases of cordierite from single-crystal
535 X-ray diffraction to 15 GPa. American Mineralogist, 100, 1821-1833.

536 García-Moreno, O., Corretgé, L.G., and Castro, A. (2007) Processes of assimilation in the genesis of
537 cordierite leucomonzogranites from the Iberian Massif: a short review. Canadian Mineralogist, 45,
538 71–85.

539 Gatta, G.D., Nestola, F., Bromiley, G.D., and Mattauch, S. (2006) The real topological configuration
540 of the extra-framework content in alkali-poor beryl: a multi-methodological study. American
541 Mineralogist, 91, 29-34.

542 Gatta, G.D., Adamo, I., Meven, M., and Lambruschi, E. (2012) A single-crystal neutron and X-ray
543 diffraction study of pezzottaite, $Cs(Be_2Li)Al_2Si_6O_{18}$. Physics and Chemistry of Minerals, 39, 829–
544 840.

545 Gatta, G.D., Lotti, P., and Tabacchi, G. (2018) The effect of pressure on open-framework silicates:
546 elastic behaviour and crystal–fluid interaction. Physics and Chemistry of Minerals, 45, 115–138.

547 Gibbs, G.V., Breck, D.W., and Meagher, E.P. (1968) Structural refinement of hydrous and anhydrous
548 synthetic beryl, $Al_2(Be_3Si_6)O_{18}$ and emerald, $Al_{1.9}Cr_{0.1}(Be_3Si_6)O_{18}$. Lithos, 1, 275–285.

549 Gonzalez-Platas, J., Alvaro, M., Nestola, F., and Angel, R. (2016) *EosFit7-GUI*: a new graphical
550 user interface for equation of state calculations, analyses and teaching. Journal of Applied
551 Crystallography, 49, 1377–1382.

552 Hejny, C., Miletich, R., Jasser, A., Schouwink, P., Crichton, W., and Kahlenberg, V. (2012) Second
553 order $P\bar{6}c2$-$P31c$ structural transition and structural crystallography of the cyclosilicate benitoite,
554 $BaTiSi_3O_9$, at high pressure. American Mineralogist, 97, 1747-1763.

555 Hess, P.C. (1969) The Metamorphic Paragenesis of Cordierite in Pelitic Rocks. Contributions to
556 Mineralogy and Petrology, 24, 191-207.

557 Hofmeister, A.M., Hoering, T.C., and Virgo, D. (1987) Vibrational spectroscopy of beryllium
558 aluminosilicates: Heat capacity calculations from band assignments. Physics and Chemistry of
559 Minerals, 14, 205–224.

560 Jacobsen, S.D., Holl, C.M., Adams, K.A., Fischer, R.A., Martin, E.S., Bina, C.R., Lin, J.F.,
561 Prakapenka, V.B., Kubo, A., and Dera, P. (2008) Compression of single-crystal magnesium oxide
562 to 118 GPa and a ruby pressure gauge for helium pressure media. American Mineralogist, 93,
563 1823–1828.

564 Kim, C.C., Bell, M.I., and McKeown, D.A. (1995) Vibrational analysis of beryl ($Be_3Al_2Si_6O_{18}$) and
565 its constituent ring (Si_6O_{18}). Physica B: Condensed Matter, 205, 193–208.

566 King, H.E., and Finger, L.W. (1979) Diffracted beam crystal centering and its application to high-
567 pressure crystallography. Journal of Applied Crystallography, 12, 374–378.

568 Klein, C., and Philpotts, A.R. (2012) Earth Materials: Introduction to Mineralogy and Petrology.
569 Cambridge University Press, UK, 552 p. (ISBN 0521761158).

570 Kolesov, A., and Geiger, C.A. (2000) Cordierite II. The role of CO_2 and H_2O. American Mineralogist,
571 85, 1265-1274.

572 Lambruschi, E., Gatta, G.D., Adamo, I., Bersani, D., Salvioli-Mariani, E., and Lottici, P.P. (2014)
573 Raman and structural comparison between the new gemstone pezzottaite $Cs(Be_2Li)Al_2Si_6O_{18}$ and
574 Cs-beryl. Journal of Raman Spectroscopy, 45, 993–999.

575 Malcherek, T., Domeneghetti, M.C., Tazzoli, V., Ottolini, L., McCammon, C., and Carpenter, M.A.
576 (2001) Structural properties of ferromagnesian cordierites. American Mineralogist, 86, 66-79.

577 Mashkovtsev, R.I., and Thomas, V.G. (2005) Nitrogen atoms encased in cavities within the beryl
578 structure as candidates for qubits. Applied Magnetic Resonance, 28, 401–409.

579 Miletich, R., Allan, D.R., and Kuhs, W.F. (2000) High-Pressure Single-Crystal Techniques. Reviews
580 in Mineralogy and Geochemistry, 41, 445–519.

581 Miletich, R., Gatta, G.D., Willi, T., Mirwald, P.W., Lotti, P., Merlini, M., Rotiroti, N., and Loerting,
582 T. (2014) Cordierite under hydrostatic compression: Anomalous elastic behavior as a precursor
583 for a pressure-induced phase transition. American Mineralogist, 99, 479-492.

584 Miletich, R., Scheidl, K.S., Schmitt, M., Moissl, A.P., Pippinger, T., Gatta, G.D., Schuster, B., and
585 Trautmann, C. (2014) Static elasticity of cordierite I: Effect of heavy ion irradiation on the
586 compressibility of hydrous cordierite. Physics and Chemistry of Minerals, 41, 579-591.

587 Moroz, I., Roth, M., Boudeulle, M., and Panczer, G. (2000) Raman microspectroscopy and
588 fluorescence of emeralds from various deposits. Journal of Raman Spectroscopy, 31, 485–490.

589 O'Bannon, E., and Williams, Q. (2016) Beryl-II, a high-pressure phase of beryl: Raman and
590 luminescence spectroscopy to 16.4 GPa. Physics and Chemistry of Minerals, 43, 671–687.

591 Palatinus, L., and Chapuis, G. (2007) SUPERFLIP—A Computer Program for the Solution of Crystal
592 Structures by Charge Flipping in Arbitrary Dimensions. Journal of Applied Crystallography, 40,
593 786-790.

594 Palke, A.C., Henling, L.M., Rossman, G.R., Sun, Z., Renfro, N., Kampf, A.R., Thu, K., Myo, N.,
595 Wongrawang, P., and Weeramonkhonlert, V. (2021) Johnkoivulaite, $Cs(Be_2B)Mg_2Si_6O_{18}$, a new
596 mineral of the beryl group from the gem deposits of Mogok, Myanmar. American Mineralogist,
597 106, 1844-1851.

598 Petrícek, V., Dusek, M., and Palatinus, L. (2014) Crystallographic Computing System JANA2006:
599 General features. Zeitschrift für Kristallographie - Crystalline Materials, 229, 345-352.

600 Prencipe, M., Scanavino, I., Nestola, F., Merlini, M., Civalleri, B., Bruno, M., and Dovesi, R. (2011)
601 High-pressure thermo-elastic properties of beryl ($Al_4Be_6Si_{12}O_{36}$) from ab initio calculations, and
602 observations about the source of thermal expansion. Physics and Chemistry of Minerals, 38, 223–
603 239.

604 Prince, E. (2006) International Tables for Crystallography Volume C: Mathematical, physical and
605 chemical tables. International Union of Crystallography, Chester, UK.

606 Redfern, S.A.T., Salje, E.K.H., Maresch, W., and Schreyer, W. (1989) X-ray powder diffraction and
607 infrared study of the hexagonal to orthorhombic phase transition in K-bearing cordierite. American
608 Mineralogist, 74, 1293-1299.

Scheidl, K.S., Gatta, G.D., Pippinger, T., Schuster, B., Trautmann, C., and Miletich, R. (2014) Static elasticity of cordierite II: effect of molecular CO_2 channel constituents on the compressibility. Physics and Chemistry of Minerals, 41, 617-631.

Scheidl, K.S., Miletich, R., Kurnosov, A., Trots, D.M., Boffa Ballaran, T., and Angel, R.J. (2016) Extending the single-crystal quartz pressure gauge up to hydrostatic pressure of 19 GPa. Journal of Applied Crystallography, 49, 2129–2137.

Spear, F.S. (1993) Metamorphic Phase Equilibria and Pressure – Temperature – Time Paths. Monograph. Mineralogical Society of America, Washington, D.C. (2nd printing with corrections 1995), 799 p., ISBN 0-939950-34-0.

Wilson, A.J.C., and Prince, E. (1999) International Tables for Crystallography, Vol. C, 2nd ed., Kluwer Academic Publishers, Dordrecht, The Netherlands.

Yakubovich, O.V., Pekov, I.V., Steele, I.M., Massa, W., and Chukanov, N.V. 2009) Alkali metals in beryl and their role in the formation of derivative structural motifs: Comparative crystal chemistry of vorobyevite and pezzottaite. Crystallographic Reports, 54, 399–412.

Table 1. Bulk moduli K_0 and axial moduli M_0 and their pressure derivatives K' and M' obtained for fits of the Birch-Murnaghan equation-of-state. For better comparability, the base vector of the beryl subcell was used for the *a*-axis of both polymorphic forms; volumes therefore correspond to that of the beryl subcell.

	P-range (GPa)	EoS-type*	X_0	K_0, M_0	K', M'
*Volume***					
	0.457-3.553	BM-3	V_0= 702.7(2) Å^3	K_0 = 152(7) GPa	K' = -2(3)
	0.457-3.553	BM-3 (K'=fix)	V_0= 702.8(2) Å^3	K_0 = 148(2) GPa	K' = 0
	4.765-8.414	BM-3	V_0= 721(5) Å^3	K_0 = 68(14) GPa	K'= 5(3)
	4.765-8.414	BM-2 (K'=4)	V_0= 718.2(5) Å^3	K_0 = 75.5(9) GPa	K' = 4
*a-axis***					
	0.457-3.553	BM-3	a_0= 9.4736(20) Å	M_0 = 441(43) GPa	M' = 10(20)
	0.457-3.553	BM-3 (M'=fix)	a_0= 9.4728(10) Å	M_0 = 462(9) GPa	M' = 0
	4.765-8.414	BM-3	a_0= 9.527(17) Å	M_0 = 257(48) GPa	M' = 13(9)
	4.765-8.414	BM-2 (M'=12)	a_0= 9.525(3) Å	M_0 = 263(4) GPa	M' = 12
c-axis					
	0.457-3.553	BM-3	c_0= 9.0445(2) Å	M_0 = 423(34) GPa	M' = -8(14)
	0.457-3.553	BM-3 (M'=fix)	c_0= 9.0444(9) Å	M_0 = 411(7) GPa	M' = 0
	4.765-8.414	BM-3	c_0= 9.177(23) Å	M_0 = 131(40) GPa	M' = 21(10)
	4.765-8.414	BM-2 (M'=12)	c_0= 9.144(3) Å	M_0 = 173(2) GPa	M' = 12

* BM-3 = third-order Birch-Murnaghan EoS; BM-2 = second-order Birch-Murnaghan EoS

** of the beryl subcell ($V_{subcell} = V_{LP\text{-}phase}$; $V_{subcell} = 1/3\ V_{HP\text{-}phase}$; $a_{subcell} = a_{LP\text{-}phase}$; $a_{subcell} = 1/\sqrt{3}\ a_{HP\text{-}phase}$)

Table S1 (deposited). Experimental details of the various DAC high-pressure loadings.

Application	Raman spectra	XRD intensities (crystal structures)	XRD lattice parameters (equation of state)
DAC type	ETH	ETH	ETH
Anvil type and culet C	BA, C=0.6 mm	BA, C=0.6 mm	BA, C=0.6 mm
Thickness of pre-indented gasket	83 ± 2 µm	90± 2 µm	105 ± 2 µm
Pressure-chamber diameter	225 ± 5 µm	260± 5 µm	270 ± 5 µm
Sample crystal (johnkoivulaite)	70 × 70 × 40 μm^3	220 × 130 × 40 μm^3	150 × 110 × 40 μm^3
XRD pressure calibrant (quartz)	-	-	90 × 55 × 40 μm^3
Optical pressure sensor	ruby	ruby	ruby
Pressure-transmitting medium	argon	4:1 methanol-ethanol	4:1 methanol-ethanol
Applied pressures	0.0001 to 10.19 GPa	1.65, 6.50 GPa	0.45 to 8.42 GPa

Table S2 (deposited). Experimental details of the single-crystal X-ray structure investigations (crystal data, intensity data collection, data processing and structure refinements). Statistical parameters as defined by the *JANA2006* suite (Petricek et al. 2014).

P (GPa)	0.0001	1.65(6)	6.50(5)
Unit-cell parameters	a = 9.470(1) Å	a = 9.450(1) Å	a = 16.130(2) Å
	c = 9.050(3) Å	c = 9.010(3) Å	c = 8.850(2) Å
	V = 702.9(2) Å^3	V = 696.8(3) Å^3	V = 1994.1(6) Å^3
Space group	*P*6/*mcc* (192)	*P*6/*mcc* (192)	$P\bar{3}c1$ (165)
Z [$Cs(Be_2B)Mg_2Si_6O_{18}$]	2	2	6
Scans	ω = 0.5°	ω = 0.5°	ω = 0.5°
sinθ/λ	≤ 0.939 Å^{-1}	≤ 0.799 Å^{-1}	≤ 0.812 Å^{-1}
	-17 ≤ h ≤ +17	9 ≤ h ≤ +9	-20 ≤ h ≤ +16
	-17 ≤ k ≤ +10	-5 ≤ k ≤ +6	-20 ≤ k ≤ +24
	-16 ≤ l ≤ +16	-13 ≤ l ≤ +9	-13 ≤ l ≤ +8
Measured reflections	56397	2517	7907
Unique refl. I_o >0σ(I_o)	859	390	1763
Unique refl. I_o >3σ(I_o)	785	284	540
Refined parameters	33	30	55
R_{eq}	0.0297	0.065	0.0957
R(F) with I_o >3σ(I_o)	0.0136	0.0441	0.0560
R(F) with I_o >0σ(I_o)	0.0157	0.0698	0.2607
wR(*F*) with I_o >3σ(I_o)	0.0209	0.0518	0.0448
wR(*F*) with I_o >0σ(I_o)	0.0211	0.0528	0.0534
Residuals (e^-/Å^3)	-0.30, +0.65	-1.19, +1.15	-2.59, +2.45

Table S3 (deposited). Fractional atomic coordinates and atomic displacement parameters (U^{ij}, Å^2).

0.0001 GPa	***s.o.f***	***x***	***y***	***z***	***Ueq or Uiso***	
Cs	*0.808(2) Cs, 0.192(2) K*	0	0	1/4	*0.02399(6)*	
Si	*1*	*0.62459(2)*	*0.72092(2)*	1/2	*0.00516(6)*	
Mg	*0.860(4) Mg, 0.140(4) Fe*	1/3	2/3	3/4	*0.00727(11)*	
Be	*0.72(7) Be, 0.28(7) B*	1/2	1/2	3/4	*0.0059(4)*	
O1	*1*	*0.51954(5)*	*0.64490(5)*	*0.64777(5)*	*0.01248(12)*	
O2	*1*	*0.78428(7)*	*0.70078(8)*	1/2	*0.01390(17)*	
	U^{11}	***U^{22}***	***U^{33}***	***U^{12}***	***U^{13}***	***U^{23}***
Cs	0.02764(7)	0.02764(7)	0.01669(7)	0.01382(4)	0	0
Si	0.00464(8)	0.00434(8)	0.00648(8)	0.00222(6)	0	0
Be	0.0062(5)	0.0062(5)	0.0057(5)	0.0034(4)	0	0
Mg	0.00726(15)	0.00726(15)	0.00728(17)	0.00363(7)	0	0
O1	0.01336(16)	0.01016(14)	0.01341(14)	0.00549(12)	0.00709(11)	0.00204(11)
O2	0.00865(19)	0.0129(2)	0.0241(3)	0.00827(17)	0	0
1.65 GPa	***s.o.f***	***x***	***y***	***z***	***Ueq or Uiso***	
Cs	0.818(6) Cs, 0.182(6) K	0	0	1/4	0.0253(5)	
Si	1	0.6243(2)	0.7209(2)	1/2	0.0079(7)	
Mg	0.857(11) Mg, 0.143(11) Fe	1/3	2/3	3/4	0.0096(9)	
Be	0.69(14) Be, 0.31(14) B	1/2	1/2	3/4	0.005(2)	
O1	1	0.5188(4)	0.6449(4)	0.6482(3)	0.0147(15)	
O2	1	0.7837(6)	0.7008(6)	1/2	0.016(2)	
	U^{11}	***U^{22}***	***U^{33}***	***U^{12}***	***U^{13}***	***U^{23}***
Cs	0.0294(6)	0.0294(6)	0.0171(7)	0.0147(3)	0	0
Si	0.0076(9)	0.0075(9)	0.0083(9)	0.0035(8)	0	0
O1	0.0167(18)	0.0144(19)	0.0137(18)	0.0084(15)	0.0031(14)	0.0024(14)
O2	0.013(3)	0.013(3)	0.025(3)	0.010(2)	0	0
6.50 GPa	***s.o.f***	***x***	***y***	***z***	***Ueq or Uiso***	
Cs1	0.760(15) Cs, 0.240(15) K	0	0	1/4	0.0202(2)	
Cs2	0.857(8) Cs, 0.143(8) K	2/3	1/3	0.2464(2)	0.0202(2)	
Si1	1	0.1797(4)	0.4509(4)	0.5054(5)	0.0057(3)	
Si2	1	0.1627(3)	0.2207(4)	0.5003(5)	0.0057(3)	
Si3	1	0.3942(4)	0.5092(4)	0.5076(5)	0.0057(3)	
Be1	2/3 Be, 1/3 B	0.1673(13)	0.3395(13)	0.7617(12)	0.0052(3)	
Be2	2/3 Be, 1/3 B	0.498(2)	0	3/4	0.0052(3)	
Mg1	0.975(16) Mg, 0.025(16) Fe	0	0.3324(7)	3/4	0.0086(5)	
Mg2	0.758(15) Mg, 0.242(15) Fe	0.3301(5)	0.3301(5)	3/4	0.0086(5)	
O1a	1	0.1302(8)	0.3901(8)	0.6563(10)	0.0078(5)	
O1b	1	0.1240(7)	0.3696(8)	0.3676(11)	0.0078(5)	
O1c	1	0.1889(7)	0.2706(8)	0.6595(9)	0.0078(5)	
O1d	1	0.2106(7)	0.2803(7)	0.3543(11)	0.0078(5)	
O1e	1	0.4553(7)	0.0429(8)	0.6227(11)	0.0078(5)	
O1f	1	0.4778(6)	0.0767(6)	0.3212(8)	0.0078(5)	
O2a	1	0.2895(9)	0.4944(8)	0.4687(7)	0.0078(5)	
O2b	1	0.4543(7)	0.6218(8)	0.5028(11)	0.0078(5)	
O2c	1	0.1769(7)	0.1317(8)	0.4925(10)	0.0078(5)	
	U^{11}	***U^{22}***	***U^{33}***	***U^{12}***	***U^{13}***	***U^{23}***
Cs1	0.0228(3)	0.0228(3)	0.0149(3)	0.01139(14)	0	0
Cs2	0.0228(3)	0.0228(3)	0.0149(3)	0.01139(14)	0	0

Table S4 (deposited). Selected cation-oxygen bond distances (Å).

P (GPa)	(Cs,K)	(Be,B)	Si	(Mg,Fe)
0.0001 GPa (*P*6/*mcc*)	*Cs-O2* 3.396(2) 12×	*Be-O1* 1.5872(6) 4×	*Si-O1* 1.6063(6) 2× *Si-O2* 1.6161(9) *Si-O2'* 1.6170(11)	*Mg-O1* 2.0909(7) 6×
1.65(5) GPa (*P*6/*mcc*)	*Cs-O2* 3.386(4) 12×	*Be-O1* 1.583(4) 4×	*Si-O1* 1.605(3) 2× *Si-O2* 1.610(7) *Si-O2'* 1.619(7)	*Mg-O1* 2.078(5) 6×
6.50(5) GPa ($P\bar{3}c1$)	*Cs1-O2c* 3.346(11) 6× *Cs1-O2c'* 3.433(11) 6× *Cs2-O2a* 3.143(12) 3× *Cs2-O2a'* 3.552(12) 3× *Cs2-O2b* 3.256(13) 3× *Cs2-O2b'* 3.266(13) 3×	*Be1-O1a* 1.54(3) *Be1-O1b* 1.45(2) *Be1-O1c* 1.60(2) *Be1-O1d* 1.60(2) *Be2-O1e* 1.64(2) 2× *Be2-O1f* 1.60(2) 2×	*Si1-O1a* 1.613(10) *Si1-O1b* 1.685(11) *Si1-O2a* 1.578(14) *Si1-O2b* 1.636(17) *Si2-O1c* 1.572(10) *Si2-O1d* 1.565(10) *Si2-O2c* 1.564(16) *Si2-O2c'* 1.661(17) *Si3-O1e* 1.558(15) *Si3-O1f* 1.620(10) *Si3-O2a* 1.620(16) *Si3-O2b* 1.575(12)	*Mg1-O1a* 2.003(11) 2× *Mg1-O1d* 1.940(15) 2× *Mg1-O1e* 2.075(16) 2× *Mg2-O1b* 2.054(19) 2× *Mg2-O1c* 2.136(12) 2× *Mg2-O1f* 2.158(11) 2×

Table S5 (deposited). Unit-cell parameters, *c/a* ratio, unit-cell volumes, and unit-cell volume per formula unit (*V*/Z) of johnkoivulaite, in addition to the unit-cell volume of the quartz used as pressure calibrant under static hydrostatic pressures at 298 K.

V_{Qz} (Å^3)	*P* (GPa)	*a* (Å)	*c* (Å)	*c*/*a*' *	*V* (Å^3)	*V*/Z (Å^3)
111.634(4)	0.457(3)	9.4654(8)	9.0323(8)	0.9542	700.83(13)	350.41(7)
110.037(9)	1.034(8)	9.4502(5)	9.0214(4)	0.9546	697.73(8)	348.87(4)
108.188(5)	1.839(4)	9.4349(6)	9.0049(4)	0.9544	694.20(9)	347.10(5)
107.574(4)	2.118(4)	9.4298(7)	8.9983(5)	0.9542	692.94(10)	346.47(5)
106.626(8)	2.570(8)	9.4207(4)	8.9879(3)	0.9541	690.81(6)	345.40(3)
105.578(5)	3.100(5)	9.4091(5)	8.9767(4)	0.9540	688.25(7)	344.14(3)
104.732(10)	3.553(11)	9.4001(5)	8.9657(3)	0.9538	686.09(7)	343.05(3)
103.765(9)	4.098(9)	16.2622(6)	8.9515(5)	0.9534	2050.17(18)	341.70(3)
102.643(6)	4.769(7)	16.2290(5)	8.9285(4)	0.9529	2036.52(15)	339.42(3)
101.783(4)	5.313(4)	16.2003(8)	8.9067(6)	0.9523	2024.39(24)	337.40(4)
100.847(8)	5.935(8)	16.1721(14)	8.8844(5)	0.9515	2012.28(22)	335.38(4)
99.955(11)	6.558(26)	16.1403(5)	8.8610(4)	0.9509	1999.11(16)	333.19(3)
99.350(9)	6.998(21)	16.1200(7)	8.8462(5)	0.9505	1990.75(19)	331.79(3)
n.d.* *	7.50(7)	16.0972(10)	8.8306(7)	0.9502	1981.62(30)	330.27(5)
n.d.* *	8.05(6)	16.0742(7)	8.8140(6)	0.9498	1972.26(21)	328.71(3)
n.d.* *	8.41(6)	16.0534(40)	8.7998(46)	0.9493	1963.98(1.32)	327.33(22)

* $a' = a$ for $P \leq 3.553$ GPa, $a' = a/\sqrt{3}$ for $P \geq 4.098$ GPa

** n.d. = not determined; pressure was determined by the ruby-fluorescence method.

Figure 1 (colour). Series of 16 single-crystal Raman spectra recorded between 0.0001 and 10.19 GPa of a johnkoivulaite single crystal hydrostatically compressed in argon: entire spectral range 50-1250 cm^{-1} (*right*) and low-frequency spectral range between 50 and 300 cm^{-1} (*left*). Spectra of the low-*P* polymorph (< 4.0 GPa) and of the high-*P* one (>4.0 GPa) are given with different colors.

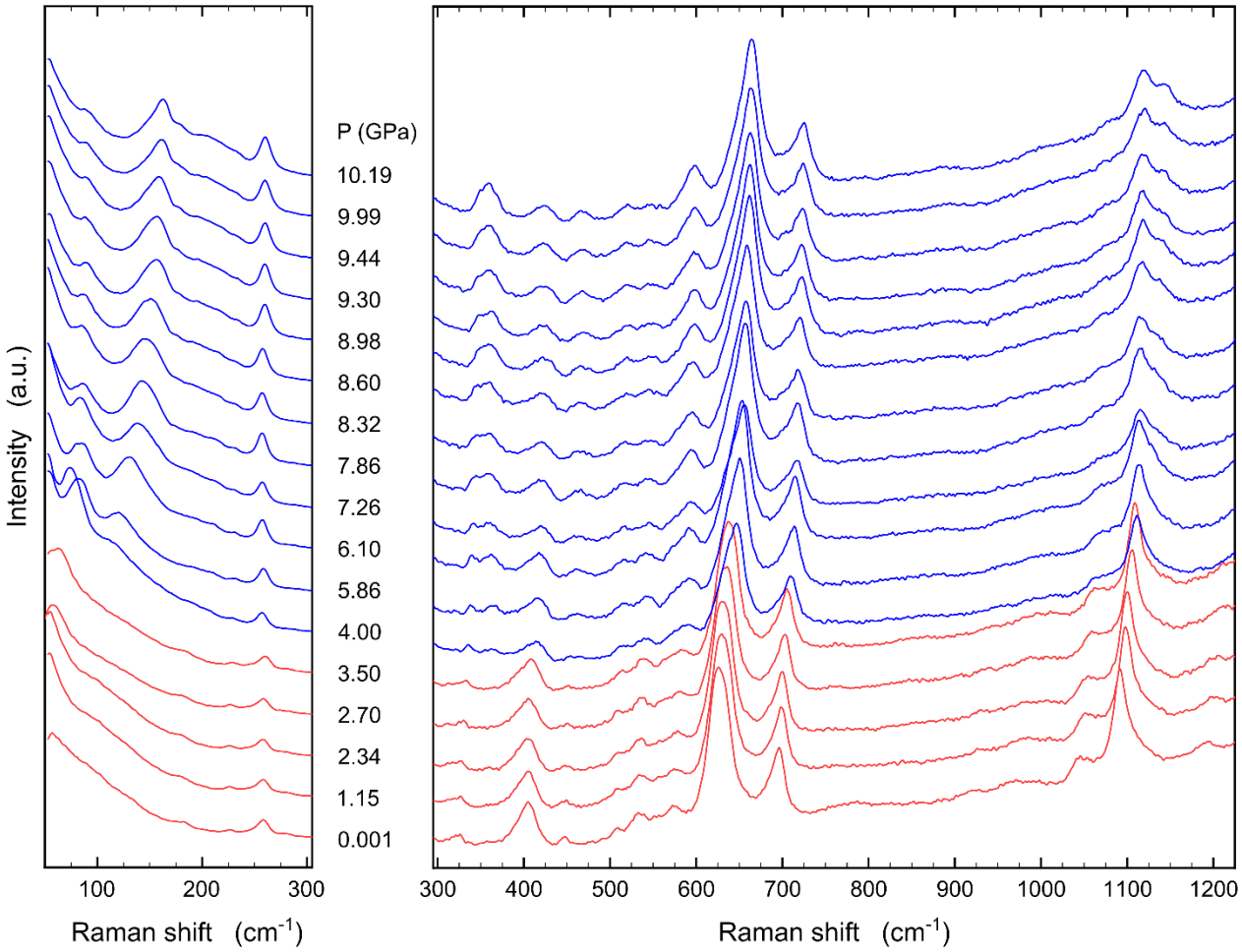

Figure 1 (B&W). Series of 16 single-crystal Raman spectra recorded between 0.0001 and 10.19 GPa of a johnkoivulaite single crystal hydrostatically compressed in argon: entire spectral range 50-1250 cm^{-1} (right) and low-frequency spectral range between 50 and 300 cm^{-1} (left). Spectra of the low-*P* polymorph (< 4.0 GPa) and of the high-*P* one (>4.0 GPa) are given with different colors.

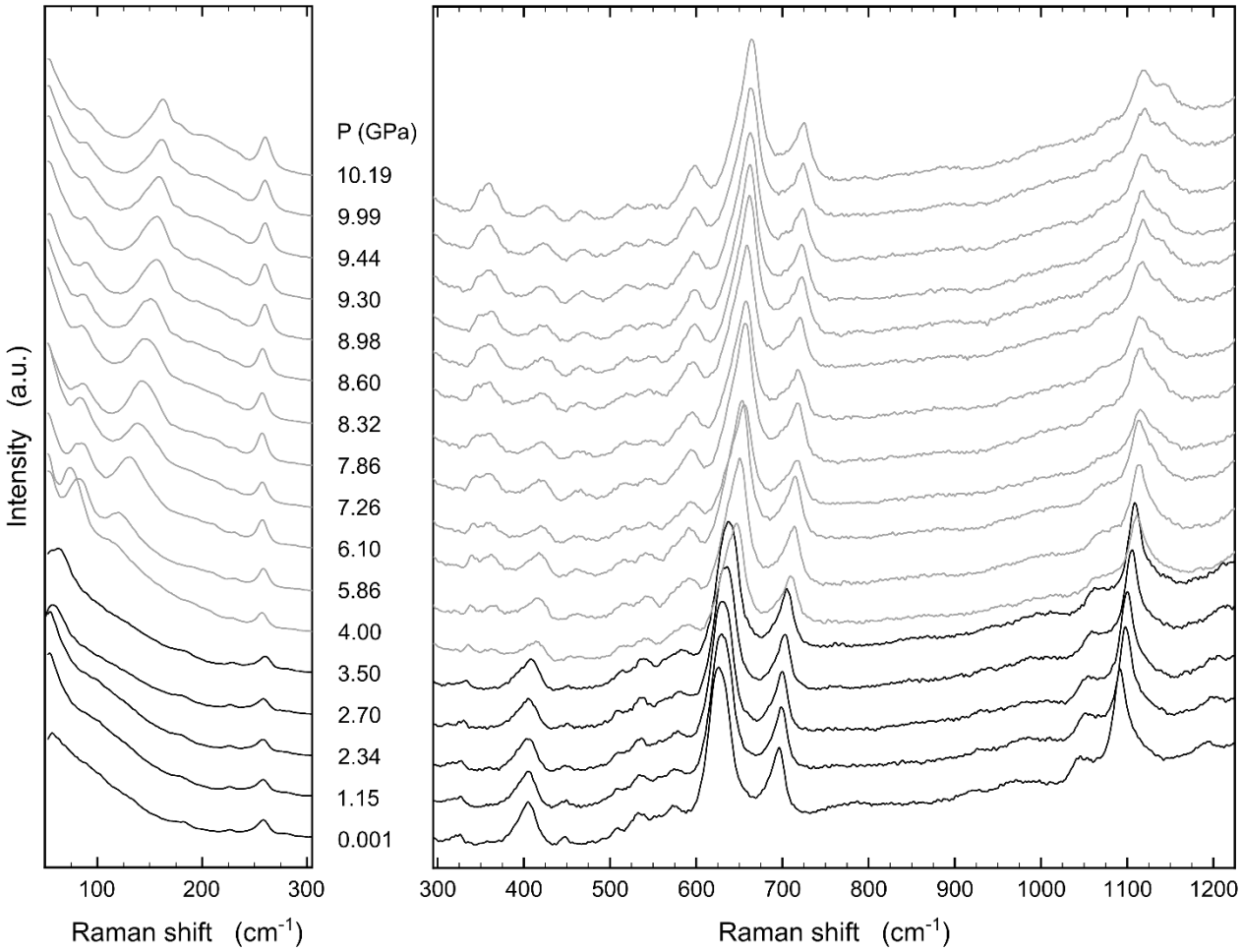

Figure 2 (colour). Pressure-induced line shifts of selected Raman modes. Values for the band position were extracted from the peak fits applied to the spectra. Errors for the band positions are within the size of the symbols, if not marked by error bars. The uncertainties for the pressure values are within ±0.06 GPa. The vertical line represents the assumed critical pressure for the transformation at ~4.0 GPa. Solid symbols represent data extracted from the compression series, empty symbols those obtained on decompression.

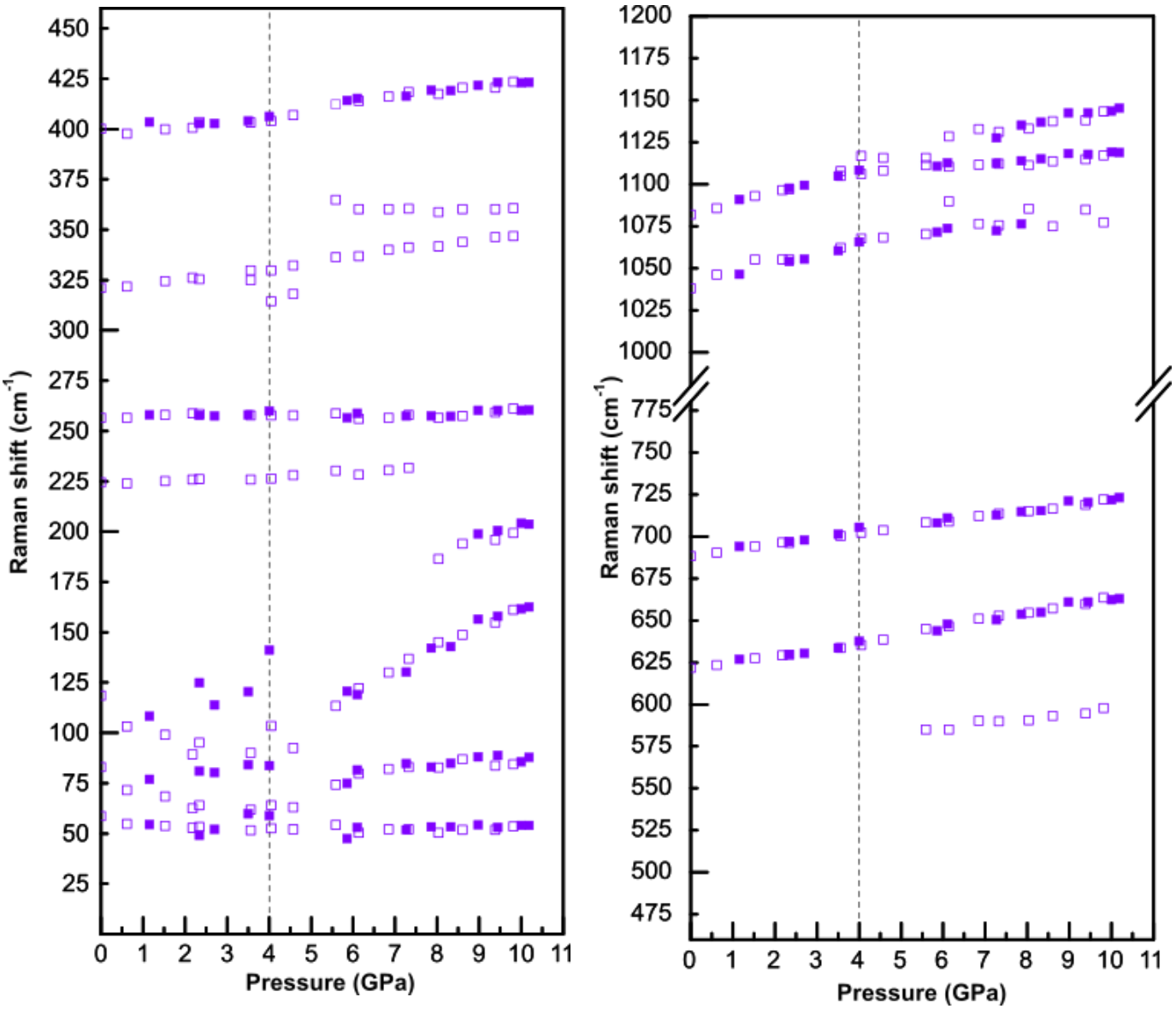

Figure 2 (B&W). Pressure-induced line shifts of selected Raman modes. Values for the band position were extracted from the peak fits applied to the spectra. Errors for the band positions are within the size of the symbols, if not marked by error bars. The uncertainties for the pressure values are within ±0.06 GPa. The vertical line represents the assumed critical pressure for the transformation at ~4.0 GPa. Solid symbols represent data extracted from the compression series, empty symbols those obtained on decompression.

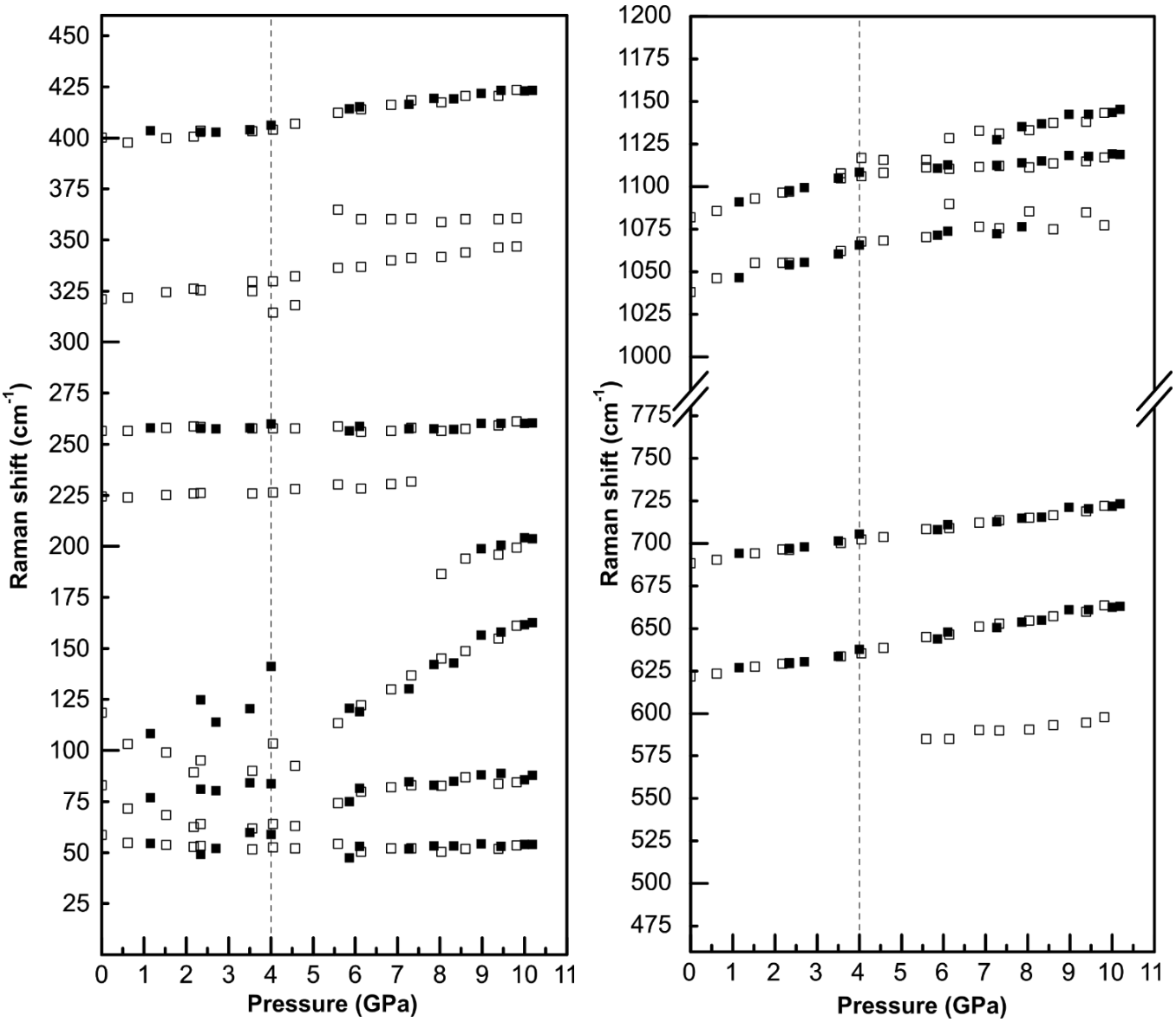

Figure 3 (colour). Pressure-dependent evolution of the unit-cell parameters *a*, *c* and the unit-cell volume *V*, along with Birch-Murnaghan EoS fits to the experimental data. The refined BM-EoS parameters are those given in Table 1.

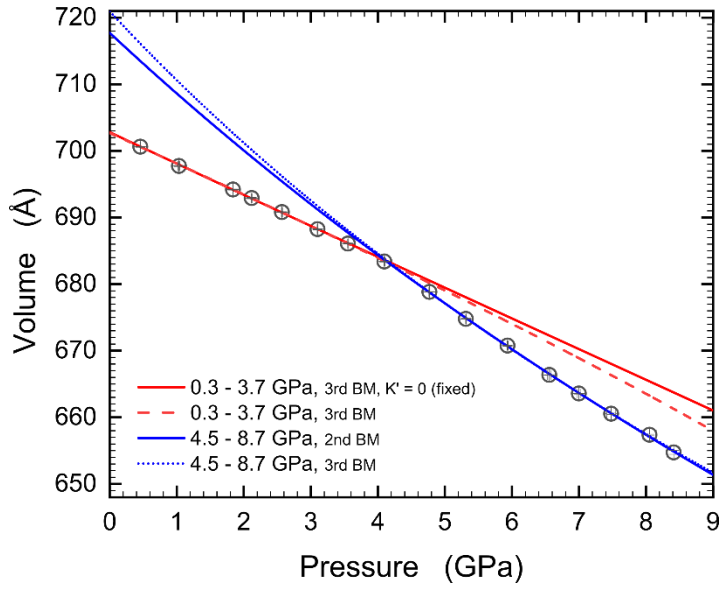

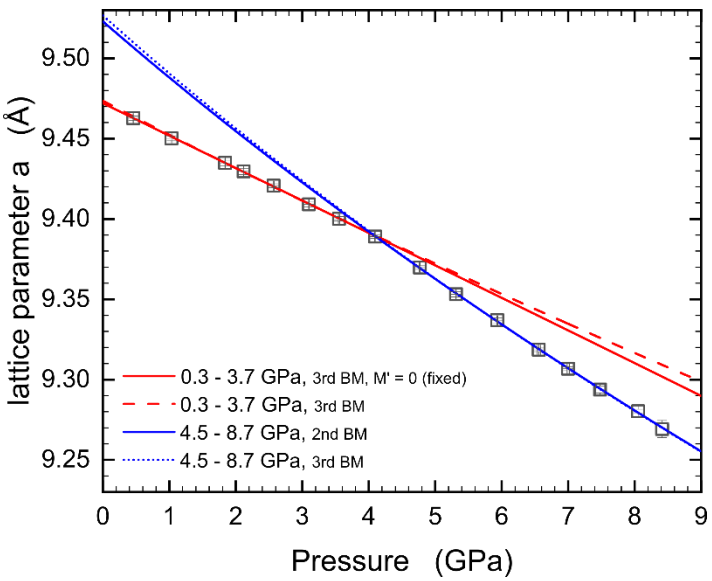

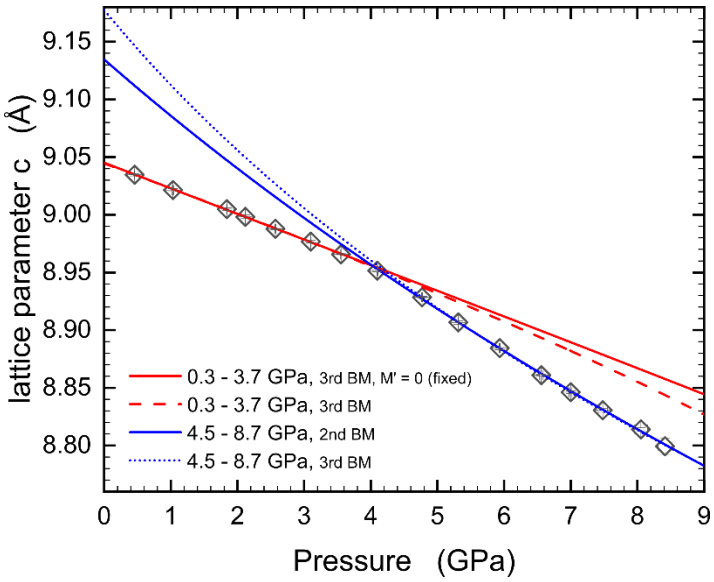

Figure 3 (B&W). Pressure-dependent evolution of the unit-cell parameters *a*, *c* and the unit-cell volume *V*, along with Birch-Murnaghan EoS fits to the experimental data. The refined BM-EoS parameters are those given in Table 1.

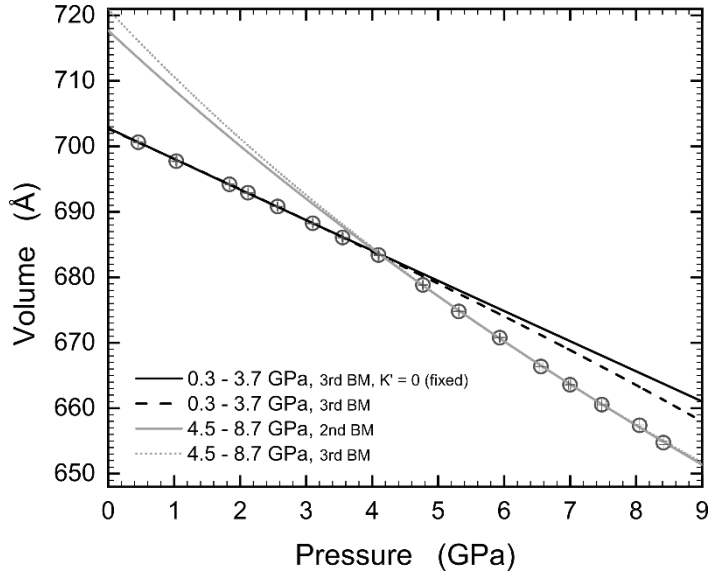

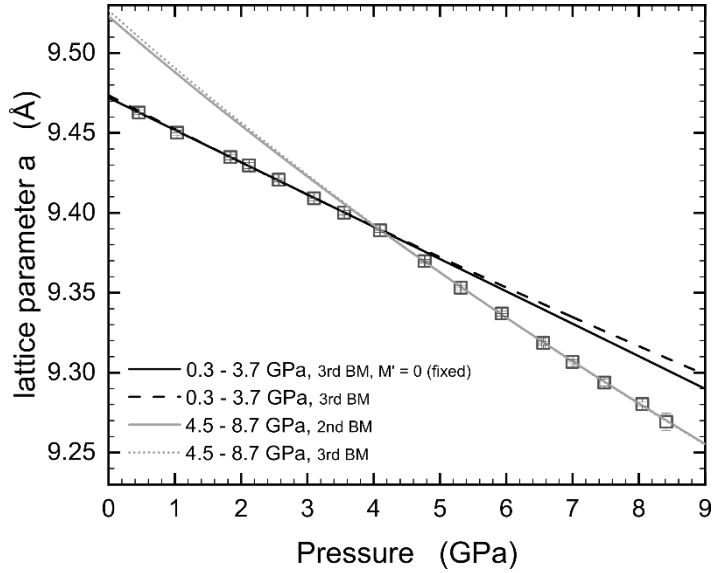

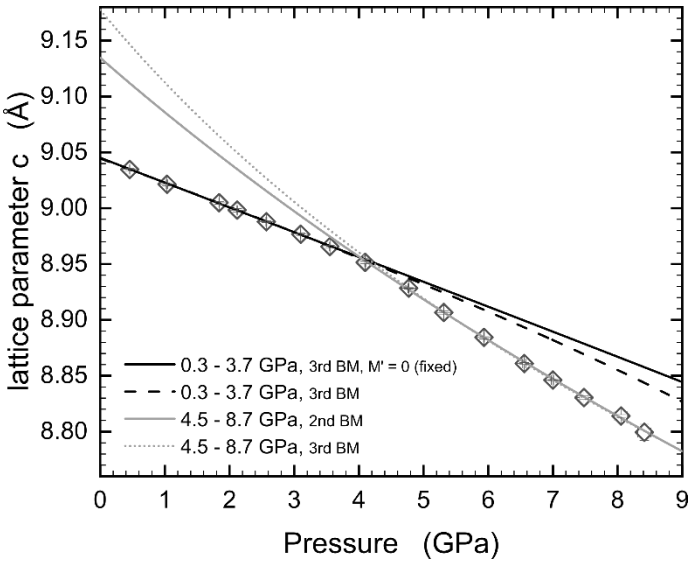

Figure 4 (colour). Metrical relationship between: (a) the unit cells of the the *P*6/*mcc* structure (beryl-type subcell) and the $P\bar{3}c1$ superstructure (with $a' = a\cdot\sqrt{3}$, $c' = c$) in a view down the *c*-axis, and (b) between the two reciprocal lattices in the reciprocal space as depicted in the *hk*0 layer in a view down the *c** direction.

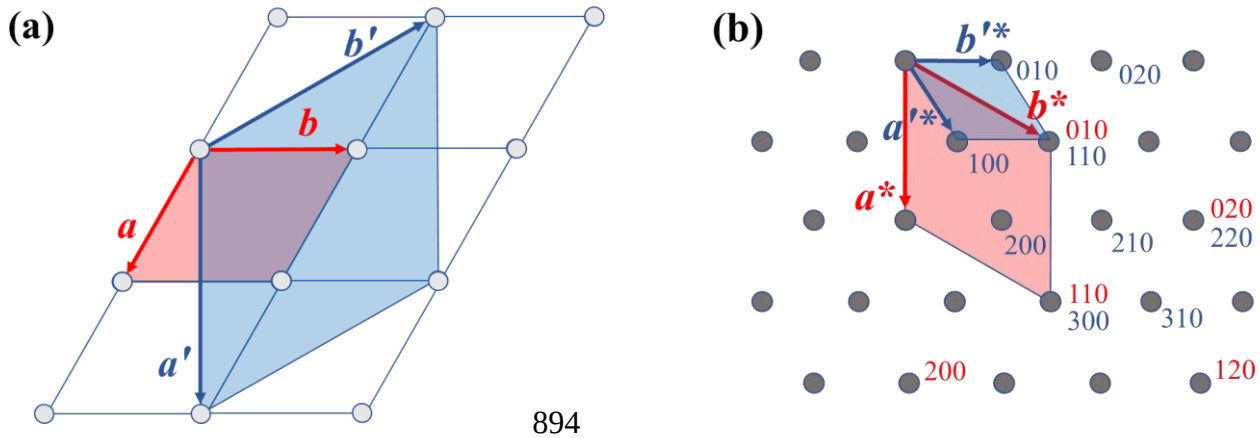

Figure 4 (B&W). Metrical relationship between: (a) the unit cells of the the *P*6/*mcc* structure (beryl-type subcell) and the $P\bar{3}c1$ superstructure (with $a' = a\cdot\sqrt{3}$, $c' = c$) in a view down the *c*-axis, and (b) between the two reciprocal lattices in the reciprocal space as depicted in the *hk*0 layer in a view down the *c** direction.

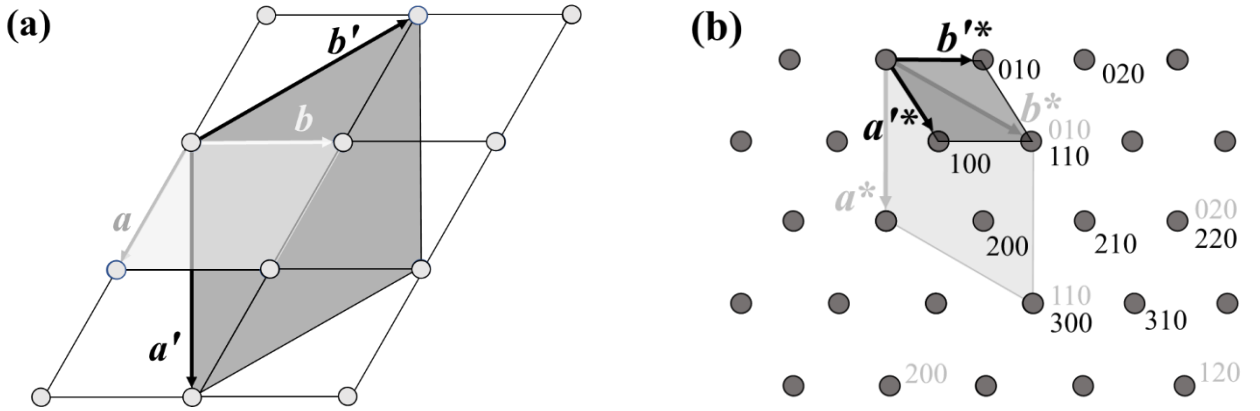

Figure 5 (colour). Reconstructed reciprocal lattice planes of the (a) *hhl* layer at P = 1.65(6) GPa, (b) *0kl* layer at P = 6.50(5) GPa, and (c) the *h0l* also at 6.50(5) GPa. The plane direction represents equivalent orientations in the reciprocal space, corresponding to the c^* (vertical arrow) and d_{110}^* (horizontal arrow) directions of the hexagonal beryl-type subcell. Indices in (a) are based on this subcell, indices in (c) correspond to the $P\bar{3}c1$ superstructure ($a' = a\cdot\sqrt{3}$, $c' = c$). Circles mark the superstructure reflections, which appear at pressures above $P_c \approx 4.0$ GPa. Apart from the sample Bragg peaks, the images show Debye rings centered in O*, which originate from scattering of the metal gasket of the diamond anvil cell.

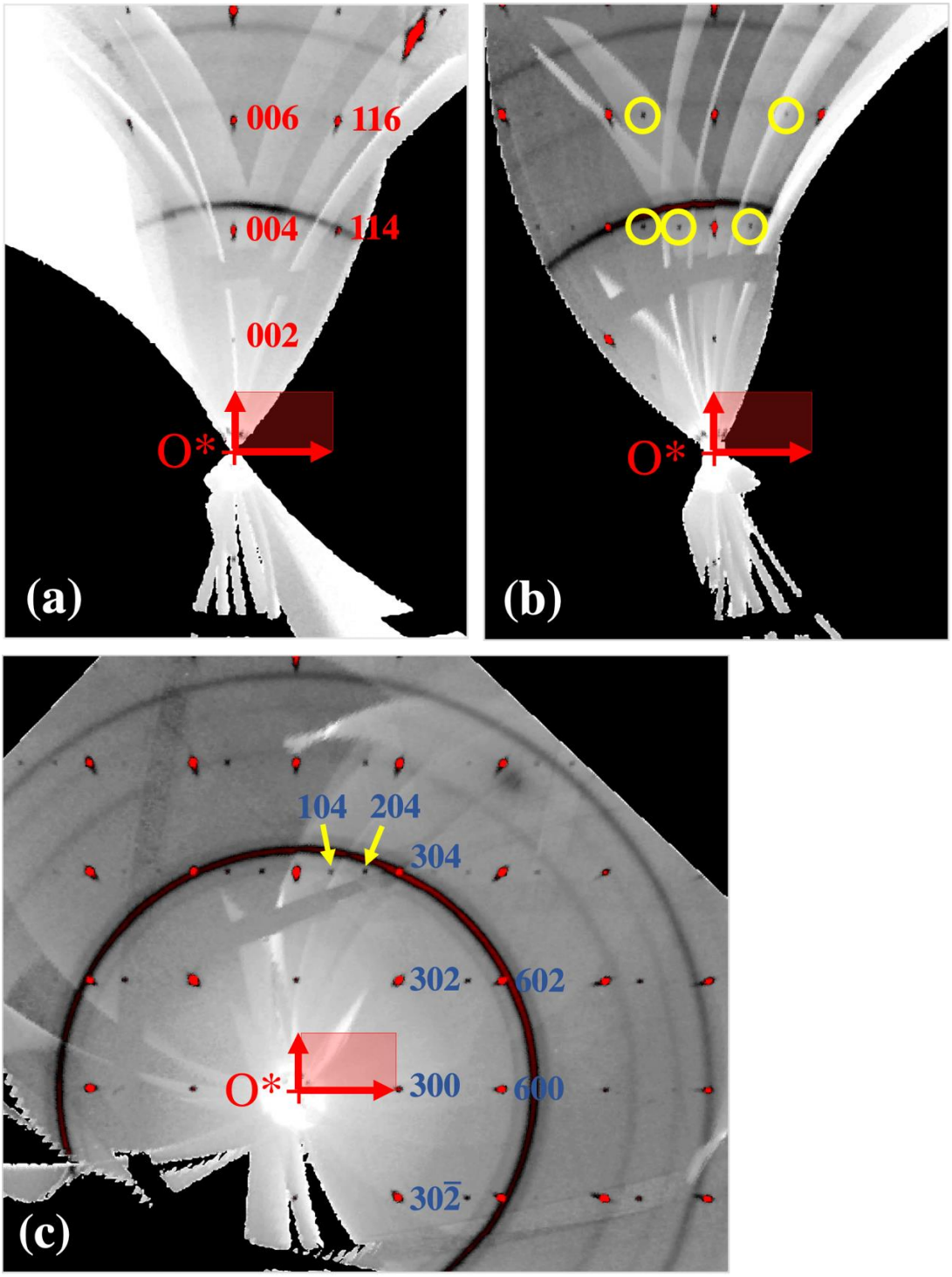

Figure 5 (B&W). Reconstructed reciprocal lattice planes of the (a) *hhl* layer at P = 1.65(6) GPa, (b) *0kl* layer at P = 6.50(5) GPa, and (c) the *h0l* also at 6.50(5) GPa. The plane direction represents equivalent orientations in the reciprocal space, corresponding to the c^* (vertical arrow) and d_{110}^* (horizontal arrow) directions of the hexagonal beryl-type subcell. Indices in (a) are based on this subcell, indices in (c) correspond to the $P\bar{3}c1$ superstructure ($a' = a\cdot\sqrt{3}$, $c' = c$). Circles mark the superstructure reflections, which appear at pressures above $P_c \approx 4.0$ GPa. Apart from the sample Bragg peaks, the images show Debye rings centered in O*, which originate from scattering of the metal gasket of the diamond anvil cell.

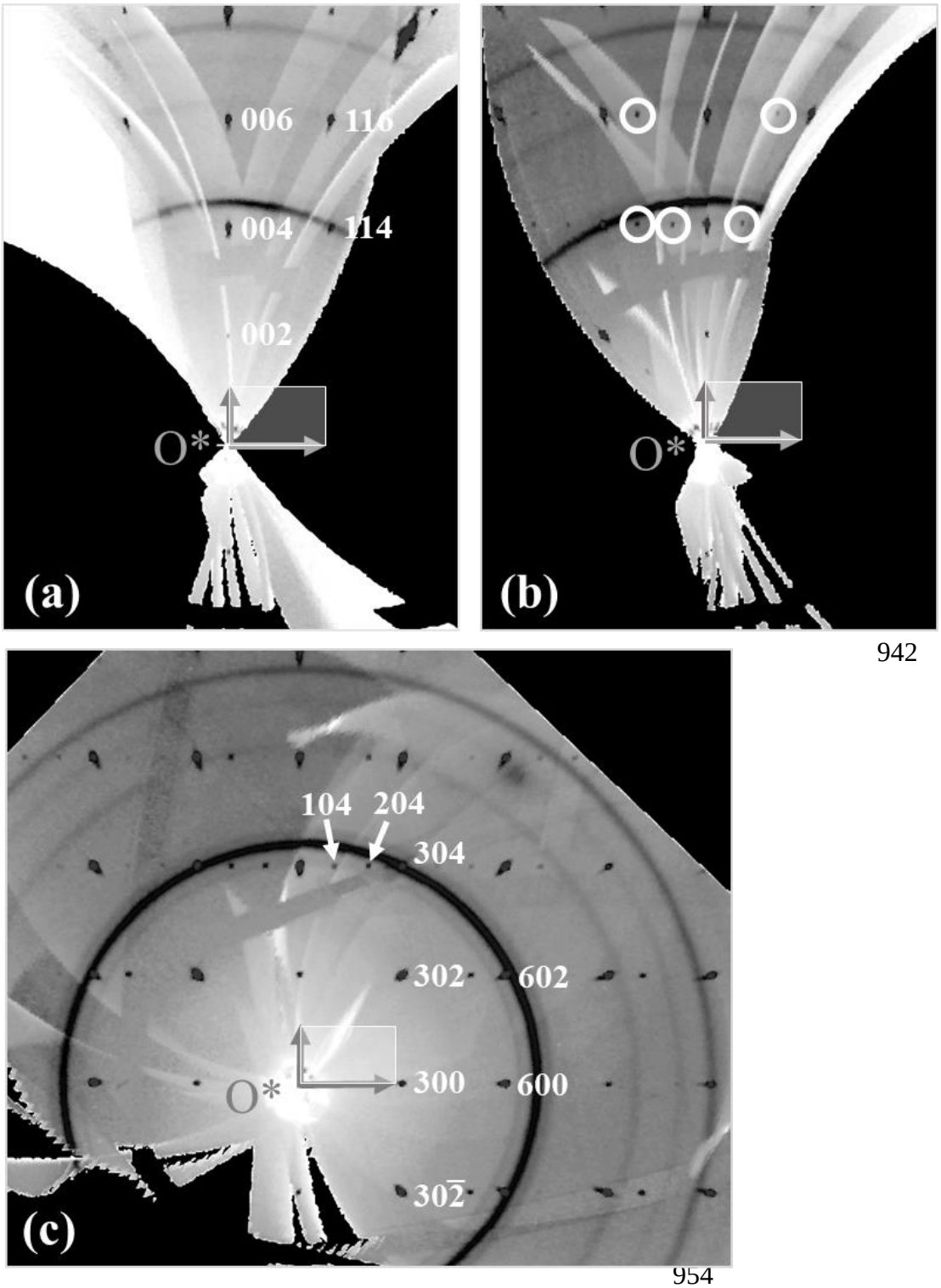

Figure 6 (colour). Di-trigonal deformation of the 12-membered ring (made by Mg,Fe-octahedra and B,Be-tetrahedra) in response to the *P*-induced phase transition in johnkoivulaite, viewed down [0001] (left side: at 0.0001 GPa; right side: at 6.50 GPa). Symmetry symbols indicate the presence of six-, three- and two-fold axis. The phase transition leads to a reduction of point symmetries from 32 (*Mg*) to .2. (*Mg*1 and *Mg*2), 222 (*Be*) to 1 (*Be*1) and .2. (*Be*2).

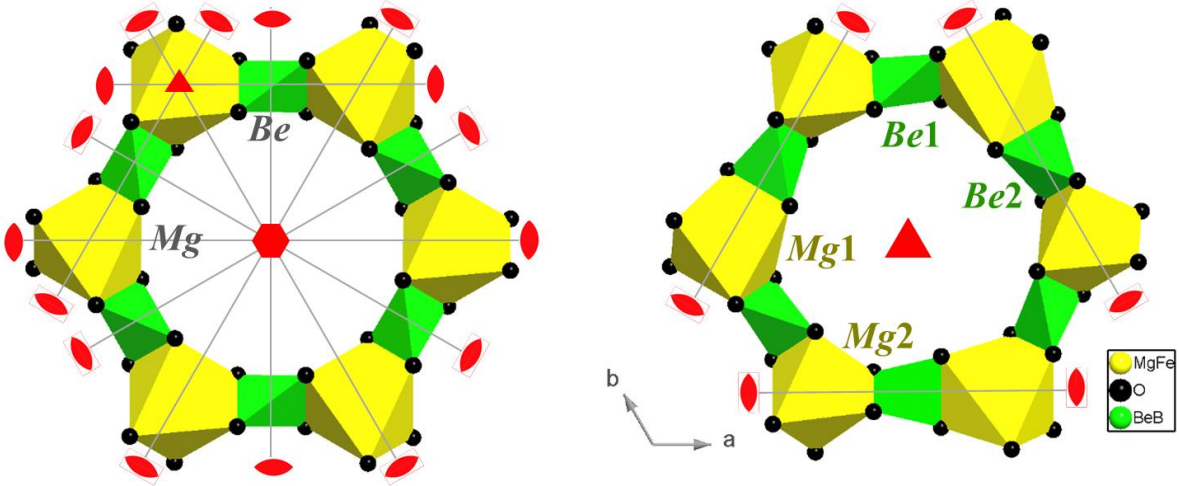

Figure 6 (B&W). Di-trigonal deformation of the 12-membered ring (made by Mg,Fe-octahedra and B,Be-tetrahedra) in response to the *P*-induced phase transition in johnkoivulaite, viewed down [0001] (left side: at 0.0001 GPa; right side: at 6.50 GPa). Symmetry symbols indicate the presence of six-, three- and two-fold axis. The phase transition leads to a reduction of point symmetries from 32 (*Mg*) to .2. (*Mg*1 and *Mg*2), 222 (*Be*) to 1 (*Be*1) and .2. (*Be*2).